Journal of Energy Storage 53 (2022) 104815

Contents lists available at ScienceDirect

Journal of Energy Storage

journal homepage: www.elsevier.com/locate/est

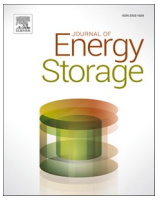

Research papers

Online diagnosis of soft internal short circuits in series-connected battery packs using modified kernel principal component analysis

Michael Schmid *, Christian Endisch

Institute of Innovative Mobility, Technische Hochschule Ingolstadt, 85049 Ingolstadt, Germany
Technische Universität München, 80333 München, Germany

ARTICLE INFO

Keywords:
Lithium-ion battery
Internal short circuit
Fault diagnosis
Fault isolation
Kernel principal component analysis
Battery safety

ABSTRACT

Safe operation of large battery storage systems requires advanced fault diagnosis that is able to detect faults and provide an early warning in the event of a fault. Since Internal Short Circuits (ISC) are the most common abuse condition leading to thermal runaway, this study addresses the early detection of incipient soft ISCs at the stage when the fault is still uncritical and does not lead to significant heat generation. The differences in cell voltages as measured by conventional battery management systems prove to be indicative features for ISC diagnosis. However, due to poor balancing and parameter variations, the cell voltage differences exhibit nonlinear variations. This work addresses this challenge with a nonlinear data model based on Kernel Principal Component Analysis (KPCA). To enable an online application in a vehicle, the present work reduces the computational complexity of the method by an optimal choice of training data. An analysis of the contribution of each cell to the fault statistics enables identification of the faulty cell. Since early-stage ISCs can exhibit a wide range of short-circuit resistances, experimental validation is performed with resistances from 10Ω to 10kΩ, which are correctly detected and isolated by the optimized cross-cell monitoring in all cases.

1. Introduction

Climate neutrality is the focus for the development of new mobility concepts [1]. In this context, Battery Electric Vehicles (BEV) and Hybrid Electric Vehicles (HEV), which today mostly have lithium-ion batteries, play a crucial role. A critical factor for customer acceptance and the adoption of BEVs and HEVs is the safety of the batteries. However, as recent studies show, serious faults in battery packs continue to occur, resulting in vehicle fire [2,3]. As Feng et al. [4] conclude, the most common causes of battery fires are Internal Short Circuits (ISC). Maleki et al. [5] confirm that the main reason for vehicle recalls are ISCs. Although the use of safer cell chemistries and advances in cell design can reduce the risk of ISCs occurring, the risk of cell failure cannot be completely eliminated. For this reason, fault diagnosis is already a key component of battery management systems [6,7]. Development is moving beyond this to more advanced fault diagnosis techniques [8].

1.1. Literature review

Early detection of ISCs has developed into a research discipline of its own. Lai et al. [11] differentiate ISC detection methods based on a vertical and a horizontal comparison. A vertical comparison means that the cell is compared only with its own historical state. For example, a model represents the historical information about the cell [9,10]. In contrast, the horizontal approach is based on a comparison of the cells with each other, where ISCs are detected based on parameter inconsistencies. An ISC can be observed by characteristic parameter changes of the affected cell, based on which (or a combination of them) a diagnosis is made. The parameters include *cell current*, *cell voltage*, *cell temperature*, *State Of Charge (SOC)* or *Open Circuit Voltage (OCV)*, *capacity* or *Internal Resistance (IR)* [12]. In battery packs with parallel connection, the electrically parallel cells feed the short-circuit cell as it shows self-discharging behavior. Based on this current, the methods of [13–15] detect an ISC. However, these approaches are only applicable to parallel cells and requires single cell current sensors, such as those available in intelligent battery systems [16,17]. In contrast, voltage-based methods offer the advantage of not requiring additional sensors, since a voltage sensor is present in any case to maintain battery pack consistency through cell balancing. Even though cell voltages are straightforward features for ISC detection, there is the challenge of

* Corresponding author at: Institute of Innovative Mobility, Technische Hochschule Ingolstadt, 85049 Ingolstadt, Germany.
E-mail address: michael.schmid@thi.de (M. Schmid).

https://doi.org/10.1016/j.est.2022.104815
Received 31 January 2022; Received in revised form 7 April 2022; Accepted 4 May 2022
Available online 14 July 2022

setting the right thresholds [11]. Poorly balanced cells, dynamic operation, cell-to-cell variation and sensor noise complicate ISC detection. While a larger voltage difference does not always imply an ISC, a small voltage difference may indicate an ISC [18]. To avoid false alarms, direct comparison of voltage values requires a large threshold, which leads to low sensitivity to early ISCs and results in a long detection time. To address this challenge, Xia et al. [19] employ the correlation coefficient and Shang et al. [20] adopt the modified sample entropy. Yang et al. [21] employ temperature as an indicator of an ISC in addition to voltage. However, a significant temperature increase can be observed only at a later stage of an ISC [4]. The heat generated in the jelly roll can be measured on the cell surface only after a delay. Moreover, many battery packs do not have cell-specific temperature sensors. One of the most widely used features for online ISC detection is the SOC or OCV [11]. Due to the self-discharging behavior of the defective cell, the ISC are detected based on an abnormally decreasing SOC. While an ISC can be detected directly from SOC inconsistency [11,22] or OCV inconsistency [23], Xia et al. [19] and Lai et al. [24] apply the correlation coefficient to SOC difference to increase robustness. Methods based on the Remaining Charge Capacity (RCC) compare the RCC of all cells with each other during a full charge [25]. Due to the self-discharge behavior of the ISC cell, the RCC continuously increases. However, the method is only applicable during charging. An ISC is also manifested by a decrease in the IR of the affected cell. However, similar to temperature, a significant change in IR is not observed until a later phase [12]. The temperature- and SOC-related change in IR makes early detection of soft ISCs based on an IR anomaly challenging [26]. However, there are approaches that diagnose ISCs using Electrochemical Impedance Spectroscopy (EIS) [27,28]. In this context, Nakajima et al. [27] identify the phase angle as a suitable feature for ISC detection.

The aim of this study is an early detection of soft ISCs, in the phase where still no heat generation can be observed and the ISC is in the kΩ range [11,29,30]. The estimation of parameters such as the SOC, OCV, or cell capacity is always accompanied by uncertainties. The uncertainties result from model structure, model parameterization, and sensor noise. Uncertainties in SOC estimation are also magnified by faults, since the short-circuit current of an ISC in series-connected battery packs is not measured by the current sensor. Due to these uncertainties, larger thresholds are required, resulting in longer detection time. Cell voltage, on the other hand, is a direct and instantaneous insight into the jelly roll. As we have shown in our previous studies [18,31,32], voltage differences are indeed indicative features. To address the aforementioned challenges of voltage-based ISC detection in the presence of parameter variations and poor balancing [11], we have already presented a novel nonlinear method, based on the Kernel Principal Component Analysis (KPCA) [18,32]. Originally introduced by Schölkopf et al. [33], Lee et al. [34] propose KPCA as a nonlinear extension of linear process monitoring. The comparison with existing methods from the literature has already shown the high sensitivity of the novel method [32].

1.2. Motivations and contributions

Based on the KPCA method, the present study addresses the so far unsolved problems of nonlinear cross-cell monitoring. The main contributions of this work are as follows:

- In order to reduce the computational effort of the nonlinear monitoring, a method for the optimal choice of the training data is presented. Besides the theoretical derivation of the method, a detailed analysis and discussion of the approach based on experimental data is given.
- In addition to fault detection, this work develops a method for fault isolation in the context of nonlinear monitoring with mixed kernel functions suitable for locating the faulty cell in the battery pack.
- A Pareto-optimal choice of tuning parameters finds optimized parameters that provide a low False Alarm Rate (FAR) in addition to a low Missed Detection Rate (MDR).
- To demonstrate robustness and sensitivity to soft ISCs, experimental studies are performed on a battery module with a wide range of short-circuit resistances on the order of 10Ω to 10kΩ.

1.3. Organization of the paper

The following work is organized as follows: Section 2 presents the theoretical basis for the nonlinear monitoring method. To this end, the section discusses data preprocessing, training and monitoring with the KPCA data model, efficient training data selection, and fault isolation. The experimental module test bench and ISC emulation method is presented in Section 3. Section 4 discusses the results on ISC diagnosis in terms of the optimal choice of training data and parameters, and the application to the wide range of short-circuit resistances. Section 5 summarizes the results and findings of the study.

2. Methods for the proposed ISC detection framework

In the following, the preprocessing of the data is presented and the methodology for KPCA is summarized. Based on this, modifications of the KPCA method are presented.

2.1. Preprocessing of the single cell voltages

The training data for the nonlinear data model consists of N measured voltage samples from m series-connected battery cells. The single cell voltage measurements $\boldsymbol{v}_\tau \in \mathbb{R}^m, \tau \in [1, N]$ are centered according to

$$\boldsymbol{x}_\tau = \frac{\boldsymbol{v}_\tau - \overline{v}_\tau^{\text{med}} \mathbf{1}_m}{s_\tau^{\text{med}}} \in \mathbb{R}^m \tag{1}$$

using the Outlier Robust Sample Studentization (ORSS) method [31]. The variable τ denotes data samples during the unsupervised training, t during the monitoring. $\mathbf{1}_m \in \mathbb{R}^m$ is the m-dimensional vector of all ones and $\overline{v}_\tau^{\text{med}}$ corresponds to the median of the m signals. The denominator

$$s_\tau^{\text{med}} = \sqrt{\frac{1}{m_z - 1} \sum_{c=1}^{m_z} \left(v_{\tau c} - \overline{v}_\tau^{\text{med}}\right)} \tag{2}$$

is calculated analogously to the standard deviation, but instead of the mean value of the data, the median is used. Furthermore, choosing a subset $m_z \leq m$ of signals with the smallest z-score allows for robustness to outliers. The choice of m_z is $m_z = 10$ for the present study with $m = 12$ cells. The features $\boldsymbol{x}_\tau$ can be interpreted as a point in an m-dimensional space for each instant τ. The aggregation of all instances results in the training data matrix $\boldsymbol{X} = [\boldsymbol{x}_1, \ldots, \boldsymbol{x}_\tau, \ldots, \boldsymbol{x}_N]^T \in \mathbb{R}^{N \times m}$.

For the application of PCA, the columns of $\boldsymbol{X}$, denoted as $\boldsymbol{\xi}_c = [x_{1c}, \ldots, x_{\tau c}, \ldots, x_{Nc}]^T \in \mathbb{R}^N$, are centered along the $c \in [1, m]$ dimensions [35]:

$$\zeta_c = \frac{\boldsymbol{\xi}_c - \overline{\xi}_c^{\text{train}} \mathbf{1}_N}{s_c^{\text{train}}} \in \mathbb{R}^N, \tag{3}$$

where $\overline{\xi}_c^{\text{train}}$ is the mean and s_c^{train} is the standard deviation. Each dimension c corresponds a cell within the battery pack. This data pre-

processing results in a data matrix

$$\boldsymbol{Z} = \begin{bmatrix} z_1^T \\ \vdots \\ z_\tau^T \\ \vdots \\ z_N^T \end{bmatrix} = \begin{bmatrix} z_{11} & \cdots & z_{1c} & \cdots & z_{1m} \\ \vdots & \ddots & \vdots & \ddots & \vdots \\ z_{\tau 1} & \cdots & z_{\tau c} & \cdots & z_{\tau m} \\ \vdots & \ddots & \vdots & \ddots & \vdots \\ z_{N1} & \cdots & z_{Nc} & \cdots & z_{Nm} \end{bmatrix} \in \mathbb{R}^{N \times m} \tag{4}$$

with columns $\zeta_c \in \mathbb{R}^N$:

$$\boldsymbol{Z} = [\zeta_1 \; \zeta_c \; \zeta_m]. \tag{5}$$

2.2. Training of the nonlinear data model

If the centered features z_j exhibit a linear or approximately linear relationship with independent Gaussian distributed noise, the application of linear PCA directly to the data matrix $\boldsymbol{Z}$ would suffice [31]. However, independent, Gaussian distributed noise or nonlinear relationships, as in the case of the fault features z_j for lithium-ion battery cells, require the application of a nonlinear extension of PCA, called Kernel Principal Component Analysis (KPCA) [18,36]. The rows z_τ of the data matrix $\boldsymbol{Z}$ are mapped into a high-dimensional feature space $\mathbb{F}$ using the nonlinear function

$$\widetilde{\boldsymbol{\Phi}} : \mathbb{R}^m \rightarrow \mathbb{F}, z \mapsto \eth. \tag{6}$$

According to Cover's theorem, the nonlinear input data is rather linear in a high-dimensional feature space [34,37], so linear PCA can be performed in $\mathbb{F}$. A prerequisite for the application of PCA in $\mathbb{F}$ is a centering of the mapped data $\widetilde{\boldsymbol{\Phi}}(z_\tau)$:

$$\boldsymbol{\Phi}(z_\tau) = \widetilde{\boldsymbol{\Phi}}(z_\tau) - \frac{1}{N}\sum_{\tau=1}^{N} \widetilde{\boldsymbol{\Phi}}(z_\tau). \tag{7}$$

The KPCA is based on the solution of an eigenvalue problem on the sample covariance in $\mathbb{F}$. The zero-mean mappings $\boldsymbol{\Phi}(z_\tau)$ allow a concise notation of the covariance matrix

$$\mathfrak{C} = \frac{1}{\mathrm{N}-1}\sum_{\tau=1}^{\mathrm{N}} \boldsymbol{\Phi}(z_\tau)\boldsymbol{\Phi}(z_\tau)^{\mathrm{T}}. \tag{8}$$

The eigenvalue problem to be solved is:

$$\mathfrak{C}\mathfrak{p}_s = \lambda_s \mathfrak{p}_s. \tag{9}$$

However, since the feature space can be high dimensional and even not necessarily finite [34], a direct computation of the mappings is very costly or not feasible. Schölkopf et al. [36] have presented a transformation of the eigenvalue problem using the kernel trick [38]. Here, the nonlinear mapping does not have to be computed explicitly. Instead, only scalar products of mapped points from the input space are needed. For this purpose, the eigenvectors $\mathfrak{p}_s$ are expressed as a function of the mappings $\boldsymbol{\Phi}(z_\tau)$ by means of coefficients $\alpha_{s\tau}$:

$$\mathfrak{p}_s = \sum_{\tau=1}^{N} \alpha_{s\tau}\boldsymbol{\Phi}(z_\tau) \tag{10}$$

Multiplying both sides of (9) by $\boldsymbol{\Phi}(z_l)^T, l = 1, \ldots, N$ and using (8), (10), we get the following system of N equations:

$$\frac{1}{N-1}\sum_{\tau=1}^{N} \boldsymbol{\Phi}(z_l)^T\boldsymbol{\Phi}(z_\tau)\left(\sum_{j=1}^{N} \alpha_{sj}\boldsymbol{\Phi}(z_\tau)^T\boldsymbol{\Phi}(z_j)\right) = \lambda_s \sum_{\tau=1}^{N} \alpha_{s\tau}\boldsymbol{\Phi}(z_l)^T\boldsymbol{\Phi}(z_\tau). \tag{11}$$

The mappings to $\mathbb{F}$ appear only in the form of dot products $\boldsymbol{\Phi}(z_{\tau 1})^T\boldsymbol{\Phi}(z_{\tau 2})$. The dot products are replaced by the kernel function

$$\kappa(z_{\tau_1}, z_{\tau_2}) = \boldsymbol{\Phi}(z_{\tau_1})^T\boldsymbol{\Phi}(z_{\tau_2}). \tag{12}$$

To allow a matrix notation for the system of Eq. (11), the kernel matrix

$$\boldsymbol{K} = \begin{bmatrix} \kappa(z_1, z_1) & \cdots & \kappa(z_1, z_{\tau_2}) & \cdots & \kappa(z_1, z_N) \\ \vdots & \ddots & \vdots & \ddots & \vdots \\ \kappa(z_{\tau_1}, z_1) & \cdots & \kappa(z_{\tau_1}, z_{\tau_2}) & \cdots & \kappa(z_{\tau_1}, z_N) \\ \vdots & \ddots & \vdots & \ddots & \vdots \\ \kappa(z_N, z_1) & \cdots & \kappa(z_N, z_{\tau_2}) & \cdots & \kappa(z_N, z_N) \end{bmatrix} \tag{13}$$

is introduced. Using $\boldsymbol{K}$, (11) is written as

$$\frac{1}{N-1}\boldsymbol{K}^2\boldsymbol{\alpha}_s = \lambda_s\boldsymbol{K}\boldsymbol{\alpha}_s. \tag{14}$$

The eigenvalue problem (9) transforms to the eigenvalue problem

$$\frac{1}{N-1}\boldsymbol{K}\boldsymbol{\alpha}_s = \lambda_s\boldsymbol{\alpha}_s \tag{15}$$

where the entries $\alpha_{s\tau}$ of the eigenvectors $\boldsymbol{\alpha}_s$ and corresponding eigenvalues λ_s have to be found.

The choice of the kernel function $\kappa : \mathbb{R}^m \times \mathbb{R}^m \rightarrow \mathbb{R}$ is not arbitrary. Permissible kernel functions must satisfy Mercer's theorem, resulting in a positive semi-definite kernel matrix $\boldsymbol{K}$ [39,40]. Table 1 shows a selection of commonly used kernel functions [41,42]. The linear and polynomial kernel functions κ_{lin} and κ_{poly} are global kernels, since.

$$\lim_{\|\Delta z\| \rightarrow \infty} \kappa(z + \Delta z, z) = \pm\infty \tag{16}$$

holds for a vector $z \in \mathbb{R}^m$ and a vector $z + \Delta z$ shifted by $\Delta z \in \mathbb{R}^m$ [40]. The remaining kernels are local kernel functions, since

$$\lim_{\|\Delta z\| \rightarrow \infty} \kappa(z + \Delta z, z) = 0. \tag{17}$$

By far the most widely used local kernel is the Gaussian kernel κ_{gauss}. The local kernels differ primarily in how much outliers are weighted against data close to the data center. The Student's t kernel κ_{tstud}, for example, is well suited to approximate a distribution in the presence of outliers [43]. To ensure robust behavior for more progressed ISCs, a local and a global kernel are combined, as suggested by [40]. The combination is done according to

$$\kappa_{\mathrm{mix}}(z_{\tau_1}, z_{\tau_2}) = \sum_{l=1}^{N_{\mathrm{ker}}} \omega_l \kappa_l(z_{\tau_1}, z_{\tau_2}) \tag{18}$$

with $\sum_{l=1}^{N_{\mathrm{ker}}} \omega_l \overset{!}{=} 1$.

For the derivation of the KPCA method, the mappings $\boldsymbol{\Phi}(z_\tau)$ were centered in (7), which is why the centered kernel matrix $\boldsymbol{K}$ results directly. However, since the mapping $\widetilde{\boldsymbol{\Phi}}(z_\tau)$ is not calculated explicitly, the centering cannot be performed according to (7). Substituting (7) into (11) and using (12)–(13), the condition

Table 1
Kernel types, corresponding functions and parameters: slope a, constant b, polynomial degree d, width σ [41,42].

Kernel type	$\kappa(z_{\tau 1}, z_{\tau 2})$
Linear	$\kappa_{\mathrm{lin}} = z^T_{\tau 1}\, z_{\tau 2} + b$
Polynomial	$\kappa_{\mathrm{poly}} = \left(a z^T_{\tau 1}\, z_{\tau 2} + b\right)^d$
Gauss	$\kappa_{\mathrm{gauss}} = exp\left(-\frac{1}{2\sigma^2}\| z_{\tau_1} - z_{\tau_2}\|^2\right)$
Rational Quadratic	$\kappa_{\mathrm{rq}} = 1 - \frac{\| z_{\tau_1} - z_{\tau_2}\|^2}{\| z_{\tau_1} - z_{\tau_2}\|^2 + b}$
Inverse Multiquadric	$\kappa_{\mathrm{imult}} = \left(\| z_{\tau 1} - z_{\tau 2}\|^2 + b^2\right)^{-0.5}$
Cauchy	$\kappa_{\mathrm{cauchy}} = \left(1 + \frac{1}{\sigma^2}\| z_{\tau_1} - z_{\tau_2}\|^2\right)^{-1}$
Generalized T-Student	$\kappa_{\mathrm{tstud}} = \left(1 + \| z_{\tau 1} - z_{\tau 2}\|^d\right)^{-1}$

$$\boldsymbol{K} = \widetilde{\boldsymbol{K}} - \frac{1}{N}\mathbf{1}_{N\times N}\widetilde{\boldsymbol{K}} - \frac{1}{N}\widetilde{\boldsymbol{K}}\mathbf{1}_{N\times N} + \frac{1}{N^2}\mathbf{1}_{N\times N}\widetilde{\boldsymbol{K}}\mathbf{1}_{N\times N} \tag{19}$$

is obtained. Here, $\widetilde{\boldsymbol{K}}$ denotes the non-centered kernel matrix and $\mathbf{1}_{N\times N} \in \mathbb{R}^{N\times N}$ is the matrix of all ones. The solution of the transformed eigenvalue problem (10) is done with the Singular Value Decomposition (SVD)

$$\frac{1}{N-1}\boldsymbol{K} = \boldsymbol{U}\Sigma\boldsymbol{V}^*\Big|_{\boldsymbol{K}=\boldsymbol{K}^T\geq 0} = \boldsymbol{S}\Lambda\boldsymbol{S}^T. \tag{20}$$

The diagonal matrix Λ contains the descending sorted eigenvalues of $\boldsymbol{K}/(N-1)$ on the diagonal and $\boldsymbol{S}$ contains the corresponding eigenvalues in the columns. To perform the PCA in $\mathbb{F}$, the matrix $\boldsymbol{S} = \left[\boldsymbol{S}_{\mathrm{pc}}\boldsymbol{S}_{\mathrm{res}}\right]$ is decomposed into the two orthogonal subspaces $\boldsymbol{S}_{\mathrm{pc}} \in \mathbb{R}^{N\times\gamma}$ and $\boldsymbol{S}_{\mathrm{res}} \in \mathbb{R}^{N\times(N-\gamma)}$. The principal subspace span$\{\boldsymbol{S}_{\mathrm{pc}}\}$ is spanned by the first γ eigenvectors and the residual subspace span$\{\boldsymbol{S}_{\mathrm{res}}\}$ by the remaining $N-\gamma$ eigenvectors. A similar decomposition is done for the eigenvalue matrix

$$\Lambda = \begin{bmatrix} \Lambda_{\mathrm{pc}} & \mathbf{0} \\ \mathbf{0} & \Lambda_{\mathrm{res}} \end{bmatrix} \tag{21}$$

into $\Lambda_{\mathrm{pc}} \in \mathbb{R}^{\gamma\times\gamma}$ and $\Lambda_{\mathrm{res}} \in \mathbb{R}^{(N-\gamma)\times(N-\gamma)}$. The matrix Λ_{pc} contains the γ largest eigenvalues and Λ_{res} the residual eigenvalues. Using the first γ eigenvectors $\boldsymbol{S}_{pc}$, the projection of the training data into the principal subspace is given by

$$\boldsymbol{T} = [\boldsymbol{t}_1 \ldots \boldsymbol{t}_\tau \ldots \boldsymbol{t}_N] = \boldsymbol{S}_{\mathrm{pc}}^T\boldsymbol{K} \in \mathbb{R}^{\gamma\times N}. \tag{22}$$

2.3. Online cell monitoring

For online monitoring at instant t, the vector of measured cell voltages $\mathbf{v}_t$ is preprocessed according to (1)–(3). Then, the kernel vector

$$\widetilde{\boldsymbol{k}}_t = [\,\widetilde{\kappa}(z_t, z_1) \ldots \widetilde{\kappa}(z_t, z_\tau) \ldots \widetilde{\kappa}(z_t, z_N)\,]^T \in \mathbb{R}^N, \tag{23}$$

consisting of non-centered dot products $\widetilde{\kappa}(z_t, z_\tau)$ in feature space, is calculated. The centering of the kernel vector

$$\boldsymbol{k}_t = \widetilde{\boldsymbol{k}}_t - \frac{1}{N}\widetilde{\boldsymbol{K}}\mathbf{1}_N - \frac{1}{N}\mathbf{1}_{N\times N}\widetilde{\boldsymbol{k}}_t + \frac{1}{N^2}\mathbf{1}_{N\times N}\widetilde{\boldsymbol{K}}\mathbf{1}_N \tag{24}$$

is analogous to (19). From the projection

$$\boldsymbol{t}_t = \boldsymbol{S}_{\mathrm{pc}}^T\boldsymbol{k}_t \in \mathbb{R}^\gamma \tag{25}$$

of $\boldsymbol{k}_t$ onto the kernel principal eigenvectors follow the test statistics

$$T^2(z_t) = \boldsymbol{t}_t^T\Lambda_{\mathrm{pc}}^{-1}\boldsymbol{t}_t \tag{26}$$

$$Q(z_t) = \boldsymbol{k}_t^T\boldsymbol{k}_t - \boldsymbol{t}_t^T\boldsymbol{t}_t \tag{27}$$

for the data-driven online monitoring [34]. While systematic variations in the data are learned through the principal subspace (T^2 statistic), the residual subspace (Q statistic) is associated with noise in the data [44]. Thus, the two subspaces can be interpreted as a data model and a noise model. Accordingly, the T^2 statistic is suitable for observing deviations from the model and the Q statistic for diagnosing abnormal noise behavior. Abnormal changes in the underlying system should be observable in both statistics [45]. Therefore, a data vector is considered abnormal only if both statistics are above their limit. The upper control limit for normal variation in the data are determined using a kernel density estimate of the underlying distribution [18].

2.4. Efficient selection of training data

Comparing the linear PCA monitoring [31] with the nonlinear monitoring using KPCA, the nonlinear variant shows a significantly higher computational complexity. In the linear case, the size of the covariance matrix which has to be diagonalized is $m \times m$. Thus, the matrix size depends only on the number of measured voltage signals, but not on the number N of training samples. The eigenvalue problem is solved offline. In the online procedure only a basis transformation based on the obtained offline solution is performed. This makes linear PCA monitoring a powerful and efficient tool for online fault diagnosis. Although the kernel method does not explicitly calculate the mapped data in feature space (kernel trick), the Gram matrix $\boldsymbol{K}/(N-1)$ to be diagonalized has the size $N \times N$. If the distribution of the data is to be well approximated, thousands of samples are required as training data set. Even if the Gram matrix only needs to be diagonalized offline, the centering of the test data in feature space (24) requires computational operations with $N \times N$ matrices for online monitoring. But also, the offline diagonalization of an $N \times N$ matrix quickly reaches computational limits.

Looking at the space spanned by $\{\boldsymbol{\Phi}(z_1), \ldots, \boldsymbol{\Phi}(z_N)\}$, one finds in practice that span$(\boldsymbol{\Phi}(z_1), \ldots, \boldsymbol{\Phi}(z_N))$ is a subspace of $\mathbb{F}$ with a significantly smaller dimension than N [46]. This means that the training samples are not linearly independent in $\mathbb{F}$. The dimension of the subspace span$(\boldsymbol{\Phi}(z_1), \ldots, \boldsymbol{\Phi}(z_N))$ corresponds to the rank of the kernel matrix $n = \text{ rank }(\boldsymbol{K}) \ll N$ [47]. According to Bach and Jordan [48], the rank of $\boldsymbol{K}$ decays exponentially for Gaussian kernels, so that an approximation of rank $n = O(\log N)$ can be found. For polynomially-decaying input distributions an approximation $n = O(N^{1/d+\varepsilon})$ with polynomial degree d and an arbitrary $\varepsilon > 0$ can be found [48]. In the following, a subset of mappings $\{\boldsymbol{\Phi}(z_1), \ldots, \boldsymbol{\Phi}(z_N)\}$ with linearly independent training data in $\mathbb{F}$ is identified. The procedure, based on an incomplete Cholesky decomposition, is analogous to Wang et al. [47] and similar to the feature vector procedure proposed by Baudat and Anouar [46]. Alternative approaches would be the sparse greedy approximation by Smola and Schölkopf [49] or the Nyström approximation by Williams and Seeger [50].

Let $n = \text{ rank }(\boldsymbol{K}) \ll N$ be the number of linearly independent feature vectors in $\mathbb{F}$. Then, without loss of generality, $s = 1, \ldots, n$ mappings $\boldsymbol{\Phi}(z_s)$ are chosen which form a basis for the n-dimensional subspace such that

$$\text{span}(\boldsymbol{\Phi}(z_1), \ldots, \boldsymbol{\Phi}(z_N)) \equiv \text{span}(\boldsymbol{\Phi}(z_1), \ldots, \boldsymbol{\Phi}(z_n)). \tag{28}$$

Introducing the vectors $\varphi_s = [\varphi_{s1} \ldots \varphi_{sn}]^T \in \mathbb{R}^n$, the eigenvectors are written as

$$\mathfrak{p}_s = \sum_{\tau=1}^{n} \varphi_{s\tau}\boldsymbol{\Phi}(z_\tau). \tag{29}$$

For the remaining $\tau = n+1, \ldots N$ mappings $\boldsymbol{\Phi}(z_\tau)$ exist coefficients $p_{\tau j}$, so that $\boldsymbol{\Phi}(z_\tau)$ can be expressed by

$$\boldsymbol{\Phi}(z_\tau) = \sum_{j=1}^{n} p_{\tau j}\boldsymbol{\Phi}(z_j). \tag{30}$$

For the covariance matrix follows

$$\mathfrak{C} = \frac{1}{\mathrm{N}-1}\sum_{\mathrm{j}=1}^{\mathrm{n}}\sum_{\mathrm{k}=1}^{\mathrm{n}} \mathrm{q}_{\mathrm{jk}}\boldsymbol{\Phi}(z_{\mathrm{j}})\boldsymbol{\Phi}(z_{\mathrm{k}})^{\mathrm{T}} \tag{31}$$

where

$$q_{jk} = \begin{cases} \sum_{\tau=n+1}^{N} p_{\tau j}p_{\tau k} + 1, & j = k \\ \sum_{\tau=n+1}^{N} p_{\tau j}p_{\tau k}, & j \neq k \end{cases}. \tag{32}$$

Substituting the covariance matrix and the eigenvectors in (9), we get

$$\frac{1}{N-1}\sum_{j=1}^{n}\sum_{k=1}^{n} q_{jk}\boldsymbol{\Phi}(z_j)\boldsymbol{\Phi}(z_k)^T\left(\sum_{\tau=1}^{n}\varphi_{s\tau}\boldsymbol{\Phi}(z_\tau)\right) = \lambda_s\sum_{\tau=1}^{n}\varphi_{s\tau}\boldsymbol{\Phi}(z_\tau). \tag{33}$$

Multiplying both sides of (33) by $\boldsymbol{\Phi}(z_l)^T, l=1,\ldots,n$ results in n equations, which allow a representation in dot product notation:

$$\frac{1}{N-1}\sum_{j=1}^{n}\sum_{k=1}^{n} q_{jk}\boldsymbol{\Phi}(z_l)^T\boldsymbol{\Phi}(z_j)\sum_{\tau=1}^{n}\varphi_{s\tau}\boldsymbol{\Phi}(z_k)^T\boldsymbol{\Phi}(z_\tau) = \lambda_s\sum_{\tau=1}^{n}\varphi_{s\tau}\boldsymbol{\Phi}(z_l)^T\boldsymbol{\Phi}(z_\tau). \tag{34}$$

The kernel function $\kappa(z_{\tau 1}, z_{\tau 2})$, introduced in (12), allows the notation

$$\frac{1}{N-1}\sum_{j=1}^{n}\sum_{k=1}^{n} q_{jk}\kappa(z_l,z_j)\left(\sum_{\tau=1}^{n}\varphi_{s\tau}\kappa(z_k,z_\tau)\right) = \lambda_s\sum_{\tau=1}^{n}\varphi_{s\tau}\kappa(z_l,z_\tau). \tag{35}$$

With the reduced kernel matrix

$$\boldsymbol{K}_0 = \left(\boldsymbol{K}_{\tau j}\right)_{\tau=1,\ldots,n;j=1,\ldots,n}. \tag{36}$$

and

$$\boldsymbol{Q} = \left(q_{jk}\right)_{j=1,\ldots,n;k=1,\ldots,n} \in \mathbb{R}^{n\times n} \tag{37}$$

$$\varphi_s = \left(\varphi_{s\tau}\right)_{\tau=1,\ldots,n} \in \mathbb{R}^n \tag{38}$$

follows for (35)

$$\frac{1}{N-1}\boldsymbol{K}_0\boldsymbol{Q}\boldsymbol{K}_0\varphi_s = \lambda_s\boldsymbol{K}_0\varphi_s. \tag{39}$$

The solution of (39) leads to the eigenvalue problem

$$\frac{1}{N-1}\boldsymbol{Q}\boldsymbol{K}_0\varphi_s = \lambda_s\varphi_s \tag{40}$$

with the reduced kernel matrix $\widehat{\boldsymbol{K}} = \boldsymbol{Q}\boldsymbol{K}_0 \in \mathbb{R}^{n\times n}$.

For application in fault diagnosis, the question arises how the approximation $\widehat{\boldsymbol{K}} \approx \boldsymbol{K}$ is found and the optimal choice of the n samples is made. Since $\boldsymbol{K}$ is a positive semidefinite matrix, it can always be factorized according to $\boldsymbol{K} = \boldsymbol{G}\boldsymbol{G}^T$ with the triangular matrix $\boldsymbol{G} \in \mathbb{R}^{N\times N}$ using the Cholesky decomposition [48]. The goal is to find an approximation $\widehat{\boldsymbol{G}} \in \mathbb{R}^{N\times n}$ for $\boldsymbol{G}$ that has only n columns and the associated optimal permutation matrix $\boldsymbol{P}$. The incomplete Cholesky decomposition allows finding such matrices $\boldsymbol{P}$ and $\widehat{\boldsymbol{G}}$. Unlike the ordinary Cholesky decomposition, all pivots smaller than a threshold are skipped. Given the positive semidefinite Gram matrix $\boldsymbol{K} \in \mathbb{R}^{N\times N}$ and the precision parameter η, Algorithm 1 finds a lower triangular matrix $\widehat{\boldsymbol{G}}$ and a permutation matrix $\boldsymbol{P}$ such that $\| \boldsymbol{P}\boldsymbol{K}\boldsymbol{P}^T - \widehat{\boldsymbol{G}}\widehat{\boldsymbol{G}}^T \| \leq \eta$ holds. The notation $\boldsymbol{G}_{a:b,c:d}$ denotes a submatrix of $\boldsymbol{G}$ consisting of the rows from index a to b and the columns from index c to d. The permutation matrix $\boldsymbol{P}$ is initialized with the unit matrix and the diagonal of $\boldsymbol{G}$ with the diagonal of $\boldsymbol{K}$. As long as the sum of all $N-\tau$ pivots (diagonal elements of $\boldsymbol{G}$) is greater than the threshold η, the $\tau \in [1,n]$ first columns of $\boldsymbol{G}$ are calculated successively. For this, the index j^* of the largest diagonal element is found (line 6). The permutation matrix $\boldsymbol{P}$ is actualized according to a permutation of the τ-th and j^* −th columns (line 7). In the modified Gram matrix $\boldsymbol{K}'$, the τ-th and the j^* −th columns (line 8) and rows (line 9) are permuted. Due to the permutations, the τ-th row and the j^* −th row in $\boldsymbol{G}$ with already calculated elements are also exchanged. The remaining elements of the τ-th column in $\boldsymbol{G}$ are computed in line 12. The $j \in [\tau+1, N]$ diagonal elements are computed in line 14. Instead of the precision parameter η a condition on the maximum number of columns n_{max} of $\widehat{\boldsymbol{G}}$ could be set.

Although the Algorithm 1 looks as if the complete $N\times N$ Gram matrix $\boldsymbol{K}$ has to be computed (line 2), in an efficient implementation only particular columns (line 12) or the diagonal (e.g., row 4) of the Gram matrix are needed. Thus, the total complexity of the incomplete Cholesky decomposition is $O(n^2N)$ and thus linear in N [48]. Instead of the $N\times N$ Gram matrix, only the diagonal of $\boldsymbol{K}$ has to be stored, resulting in a linear storage requirement of $O(nN)$ [48].

Algorithm 1. Incomplete Cholesky Decomposition [48].

Input: $\boldsymbol{K} \in \mathbb{R}^{N\times N}$, η

1: $\tau \leftarrow 1$
2: $\boldsymbol{K}' \leftarrow \boldsymbol{K}$
3: $\boldsymbol{P} \leftarrow \boldsymbol{I}$
4: $(\boldsymbol{G}_{jj})_{j\in[1,N]} \leftarrow (\boldsymbol{K}_{jj})_{j\in[1,N]}$
5: **while** $\sum_{j=\tau}^{N}\boldsymbol{G}_{jj} > \eta$ **do**
6: $\quad j^* \leftarrow \arg\max_{j\in[\tau,N]}\boldsymbol{G}_{jj}$
7: $\quad \boldsymbol{P}_{\tau\tau} \leftarrow 0,\ \boldsymbol{P}_{j^*j^*} \leftarrow 0,\ \boldsymbol{P}_{\tau j^*} \leftarrow 1,\ \boldsymbol{P}_{j^*\tau} \leftarrow 1$
8: $\quad \boldsymbol{K}'_{1:N,\tau} \leftrightarrow \boldsymbol{K}'_{1:N,j^*}$
9: $\quad \boldsymbol{K}'_{\tau,1:N} \leftrightarrow \boldsymbol{K}'_{j^*,1:N}$
10: $\quad \boldsymbol{G}_{\tau,1:\tau} \leftrightarrow \boldsymbol{G}_{j^*,1:\tau}$
11: $\quad \boldsymbol{G}_{\tau\tau} \leftarrow \sqrt{\boldsymbol{K}'_{\tau\tau}}$
12: $\quad \boldsymbol{G}_{\tau+1:N,\tau} \leftarrow \frac{1}{\boldsymbol{G}_{\tau\tau}}\left(\boldsymbol{K}'_{\tau+1:N,\tau} - \sum_{j=1}^{\tau-1}\boldsymbol{G}_{\tau+1:N,j}\boldsymbol{G}_{\tau j}\right)$
13: $\quad$ **for** $j = \tau+1$ to N **do**
14: $\quad\quad \boldsymbol{G}_{jj} \leftarrow \boldsymbol{K}_{jj} - \sum_{k=1}^{\tau}\boldsymbol{G}_{jk}^2$
15: $\quad$ **end for**
16: $\quad \tau \leftarrow \tau+1$
17: **end while**
18: $n \leftarrow \tau-1$
19: $\widehat{\boldsymbol{G}} \leftarrow \boldsymbol{G}_{1:N,n}$

Output: $\widehat{\boldsymbol{G}} \in \mathbb{R}^{N\times n}$, $\boldsymbol{P} \in \mathbb{R}^{N\times N}$

Based on the incomplete Cholesky decomposition, an optimal subset of training samples is found. The Gram matrix $\boldsymbol{K}$ is approximated by $\widehat{\boldsymbol{K}} = \widehat{\boldsymbol{G}}\widehat{\boldsymbol{G}}^T$ and centered using (19).

2.5. Fault isolation based on variables' contributions

The detection of a fault can be considered as the first step of a fault diagnosis procedure. The next step is to isolate the fault in the battery system. Fault isolation refers to the localization of the fault so that the detected fault can be associated with a specific cell c. While for linear PCA, approaches to calculate the fault contributions exist [31], the calculation for nonlinear PCA is challenging. It is difficult or even impossible to find an inverse mapping function $\boldsymbol{\Phi}^{-1}(\eth)$ that transforms from the high-dimensional feature space $\mathbb{F}$ to the input space $\mathbb{R}^m$. Using Lagrange's mean value theorem, Deng and Tian [51] presented an approach for Gaussian kernels to estimate the single variables' contributions. This procedure is extended below to handle the kernel functions from Table 1 as well as mixed kernels.

Let $F(z_t) \in \{\mathrm{T}^2(z_t), Q(z_t)\}$ be one of the two test statistics T^2 or Q, given in (26) and (27), respectively. For the t-th test sample $z_t = [z_{t1}\ldots z_{tc}\ldots z_{tm}]^T \in \mathbb{R}^m$ follows according to Lagrange's mean value theorem:

$$F(z_t) - F\left(z_t^0\right) = \sum_{c=1}^{m}\left(z_{tc} - z_{tc}^0\right)\frac{\partial}{\partial z_{tc}}F\left(z_t^0 + \theta\left(z_t - z_t^0\right)\right) \tag{41}$$

with the parameter $0 < \theta < 1$. Choosing ${z_t}^0 = \mathbf{0}$, without loss of generality, (41) is simplified:

$$F(z_t) = F(\mathbf{0}) + \sum_{c=1}^{m} z_{tc}\frac{\partial}{\partial z_{tc}}F(\theta z_t). \tag{42}$$

Considering (42), $F(z_t)$ is composed of a constant $F(\mathbf{0})$ and a contribution that can be assigned to one of the m variables. Therefore, the contribution $C_F(z_{tc})$ of the c-th variable to the test statistic $F(z_t)$ at time t is written as:

$$C_F(z_{tc}) = z_{tc}\frac{\partial}{\partial z_{tc}}F(\theta z_t). \tag{43}$$

For linear PCA, $F(\mathbf{0}) = 0$ holds and therefore

$$F(z_t) = \sum_{c=1}^{m} z_{tc}\frac{\partial}{\partial z_{tc}}F(\theta z_t) = \theta^2\sum_{c=1}^{m} z_{tc}\frac{\partial}{\partial z_{tc}}F(z_t) = 2\theta^2 F(z_t), \tag{44}$$

resulting in the parameter $\theta = \frac{1}{\sqrt{2}}$ [51]. In the nonlinear case, however, θ has to be calculated for each test sample z_t or a suitable common θ has to be found using the training data. For our application, already the choice of a constant $\theta = \frac{1}{\sqrt{2}}$ as in the linear case gives very good results. For a clearer notation, the calculation of the contributions is performed with the full kernel matrix $\boldsymbol{K}$. However, the calculation using the approximation $\widehat{\boldsymbol{K}} \approx \boldsymbol{K}$ follows analogously, by replacement of $\boldsymbol{K}$ with $\widehat{\boldsymbol{K}}$. With

$$T^2(z_t) = \boldsymbol{t}_t^T\Lambda_{\mathrm{pc}}^{-1}\boldsymbol{t}_t = \boldsymbol{k}_t^T\boldsymbol{S}_{\mathrm{pc}}\Lambda_{\mathrm{pc}}^{-1}\boldsymbol{S}_{\mathrm{pc}}^T\boldsymbol{k}_t, \tag{45}$$

the contribution of the c-th signal to the T^2 test statistic for test data z_t can be calculated using (43):

$$\begin{aligned} C_{T^2}(z_{tc}) &= z_{tc}\frac{\partial}{\partial z_{tc}}\left(\boldsymbol{k}_t^T\boldsymbol{S}_{\mathrm{pc}}\Lambda_{\mathrm{pc}}^{-1}\boldsymbol{S}_{\mathrm{pc}}^T\boldsymbol{k}_t\right)\Big|_{\theta z_t} \\ &= 2z_{tc}\frac{\partial \boldsymbol{k}_t^T}{\partial z_{tc}}\boldsymbol{S}_{\mathrm{pc}}\Lambda_{\mathrm{pc}}^{-1}\boldsymbol{S}_{\mathrm{pc}}^T\boldsymbol{k}_t\Big|_{\theta z_t} \end{aligned} \tag{47}$$

Similarly, with

$$Q_t(z_t) = \boldsymbol{k}_t^T\boldsymbol{k}_t - \boldsymbol{t}_t^T\boldsymbol{t}_t = \boldsymbol{k}_t^T\left(\boldsymbol{I} - \boldsymbol{S}_{\mathrm{pc}}\boldsymbol{S}_{\mathrm{pc}}^T\right)\boldsymbol{k}_t, \tag{48}$$

according to (43), follows for the contribution of the c-th variable to the Q-statistic the relation:

$$\begin{aligned} C_Q(z_{tc}) &= z_{tc}\frac{\partial}{\partial z_{tc}}\left(\boldsymbol{k}_t^T\left(\boldsymbol{I} - \boldsymbol{S}_{\mathrm{pc}}\boldsymbol{S}_{\mathrm{pc}}^T\right)\boldsymbol{k}_t\right)\Big|_{\theta z_t} \\ &= 2z_{tc}\frac{\partial \boldsymbol{k}_t^T}{\partial z_{tc}}\left(\boldsymbol{I} - \boldsymbol{S}_{\mathrm{pc}}\boldsymbol{S}_{\mathrm{pc}}^T\right)\boldsymbol{k}_t\Big|_{\theta z_t}. \end{aligned} \tag{49}$$

Here

$$\frac{\partial \boldsymbol{k}_t}{\partial z_{tc}}\Big|_{\theta z_t} = \left[\frac{\partial\kappa(\theta z_t, z_1)}{\partial z_{tc}}\cdots\frac{\partial\kappa(\theta z_t, z_\tau)}{\partial z_{tc}}\cdots\frac{\partial\kappa(\theta z_t, z_N)}{\partial z_{tc}}\right]^T, \tag{50}$$

for $\tau \in [1, N]$. $\boldsymbol{k}_t$ is the kernel vector with centered elements according to (24):

$$\begin{aligned} \kappa(\theta z_t, z_\tau) = \widetilde{\kappa}(\theta z_t, z_\tau) &- \frac{1}{N}\sum_{k=1}^{N}\widetilde{\kappa}(\theta z_t, z_k) \\ &- \frac{1}{N}\sum_{k=1}^{N}\widetilde{\kappa}(z_k, z_\tau) + \frac{1}{N^2}\sum_{l=1}^{N}\sum_{k=1}^{N}\widetilde{\kappa}(z_l, z_k). \end{aligned} \tag{51}$$

For the partial derivative of $\kappa(\theta z_t, z_\tau)$ with respect to z_{tc} follows

$$\begin{aligned} \frac{\partial\kappa(\theta z_t, z_\tau)}{\partial z_{tc}} = \frac{\partial\widetilde{\kappa}(\theta z_t, z_\tau)}{\partial z_{tc}} &- \frac{1}{N}\sum_{k=1}^{N}\frac{\partial\widetilde{\kappa}(\theta z_t, z_k)}{\partial z_{tc}} \\ &- \frac{1}{N}\sum_{k=1}^{N}\frac{\partial\widetilde{\kappa}(z_k, z_\tau)}{\partial z_{tc}} + \frac{1}{N^2}\sum_{l=1}^{N}\sum_{k=1}^{N}\frac{\partial\widetilde{\kappa}(z_l, z_k)}{\partial z_{tc}}. \end{aligned} \tag{52}$$

Since the last two terms in (54) have no dependence on z_{tc},

$$\frac{\partial\widetilde{\kappa}(z_k, z_\tau)}{\partial z_{tc}} = \frac{\partial\widetilde{\kappa}(z_l, z_k)}{\partial z_{tc}} = 0 \qquad \forall\tau, k, l \tag{53}$$

applies. Using the mixed kernel (18) results in

$$\frac{\partial\kappa(\theta z_t, z_\tau)}{\partial z_{tc}} = \sum_{l=1}^{N_{\mathrm{ker}}}\omega_l\frac{\partial\widetilde{\kappa}_l(\theta z_t, z_\tau)}{\partial z_{tc}} - \frac{1}{N}\sum_{k=1}^{N}\sum_{l=1}^{N_{\mathrm{ker}}}\omega_l\frac{\partial\widetilde{\kappa}_l(\theta z_t, z_k)}{\partial z_{tc}}. \tag{54}$$

The derivatives $\frac{\partial\widetilde{\kappa}_l(\theta z_t, z_\tau)}{\partial z_{tc}}$ and analogously the derivatives $\frac{\partial\widetilde{\kappa}_l(\theta z_t, z_k)}{\partial z_{tc}}$ are given in Table 2 for the kernel functions from Table 1. For the mixed kernel used in this study, which consists of a combination of linear and Gaussian kernel, follows:

$$\begin{aligned} &\frac{\partial\kappa(\theta z_t, z_\tau)}{\partial z_{tc}} = \\ &\omega_1\theta\left(z_{\tau c} - \frac{\theta z_{tc} - z_{\tau c}}{\sigma^2}exp\left(-\frac{1}{2\sigma^2}\parallel\theta z_t - z_\tau\parallel^2\right)\right) \\ &-\frac{\omega_2\theta}{N}\sum_{k=1}^{N}\left(z_{kc} - \frac{\theta z_{tc} - z_{kc}}{\sigma^2}exp\left(-\frac{1}{2\sigma^2}\parallel\theta z_t - z_k\parallel^2\right)\right). \end{aligned} \tag{55}$$

Using the general Eq. (54), the Eqs. (47) and (49) can be used to compute the contribution to the T^2 and Q statistics of the c-th battery cell at the t-th sampling instance.

3. Experimental procedure for the validation of the method

Fig. 1 shows the experimental setup for validation of the presented method. The test bench setup is shown schematically in Fig. 1a and the mechanical setup of the battery module, consisting of 12 cells, is shown in Fig. 1b. The cylindrical cells in 18650 format from the manufacturer Samsung have a nominal capacity of 2.5 Ah. The upper and lower cutoff voltages are 4.2 V and 2.5 V, respectively. The maximum continuous discharge and charge currents are −20A and 4A, respectively. The cells are soldered to a Printed Circuit Board (PCB) as shown in Fig. 1b. The PCB serves as a mechanical holder and is equipped with a fuse and sensors. 12 PCBs are electrically connected in series to form a module, which is located in a BINDER temperature chamber at a constant temperature of 25 °C. Electrical excitation is performed with a Chroma Module Charge/Discharge Tester. The module tester simultaneously measures the total voltage and the total current with a resolution of 2 mV and 5 mV at a frequency of 10 Hz. Single cell voltages and

Table 2

Partial derivatives $\frac{\partial}{\partial z_{tc}}\widetilde{\kappa}(\theta z_t, z_\tau)$ of the kernel functions from Table 1 for calculating the variable contributions.

$\frac{\partial}{\partial z_{tc}}\widetilde{\kappa}_{\mathrm{lin}}(\theta z_t, z_\tau)$	$= \theta z_{\tau c}$
$\frac{\partial}{\partial z_{tc}}\widetilde{\kappa}_{\mathrm{poly}}(\theta z_t, z_\tau)$	$= d\theta z_{\tau c}\left(\theta z_t^T z_\tau + c\right)^{d-1}$
$\frac{\partial}{\partial z_{tc}}\widetilde{\kappa}_{\mathrm{gauss}}(\theta z_t, z_\tau)$	$= -\frac{\theta}{\sigma^2}(\theta z_{tc} - z_{\tau c})exp\left(-\frac{1}{2\sigma^2}\frac{1}{\parallel\theta z_t - z_\tau\parallel^2}\right)$
$\frac{\partial}{\partial z_{tc}}\widetilde{\kappa}_{\mathrm{rq}}(\theta z_t, z_\tau)$	$= 2c\theta(\theta z_{tc} - z_{\tau c})\left(\parallel\theta z_t - z_\tau\parallel^2 + c\right)^{-2}$
$\frac{\partial}{\partial z_{tc}}\widetilde{\kappa}_{\mathrm{imult}}(\theta z_t, z_\tau)$	$= -\theta(\theta z_{tc} - z_{\tau c})\left(\parallel\theta z_t - z_\tau\parallel^2 + c^2\right)^{-1.5}$
$\frac{\partial}{\partial z_{tc}}\widetilde{\kappa}_{\mathrm{cauchy}}(\theta z_t, z_\tau)$	$= -\frac{2\theta}{\sigma^2}(\theta z_{tc} - z_{\tau c})\left(1 + \frac{1}{\sigma^2}\parallel\theta z_t - z_\tau\parallel^2\right)^{-2}$
$\frac{\partial}{\partial z_{tc}}\widetilde{\kappa}_{\mathrm{tstud}}(\theta z_t, z_\tau)$	$= -d\theta(\theta z_{tc} - z_{\tau c})\parallel\theta z_t - z_\tau\parallel^{d-2}\left(1 + \parallel\theta z_t - z_\tau\parallel^d\right)^{-2}$

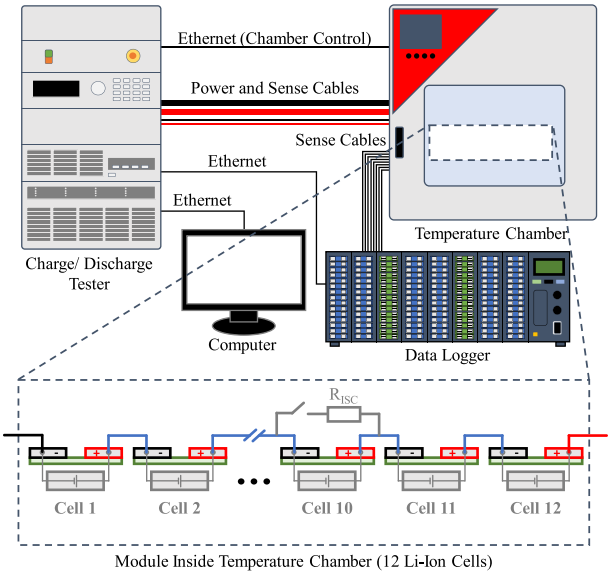

(a) Schematic setup of the test bench

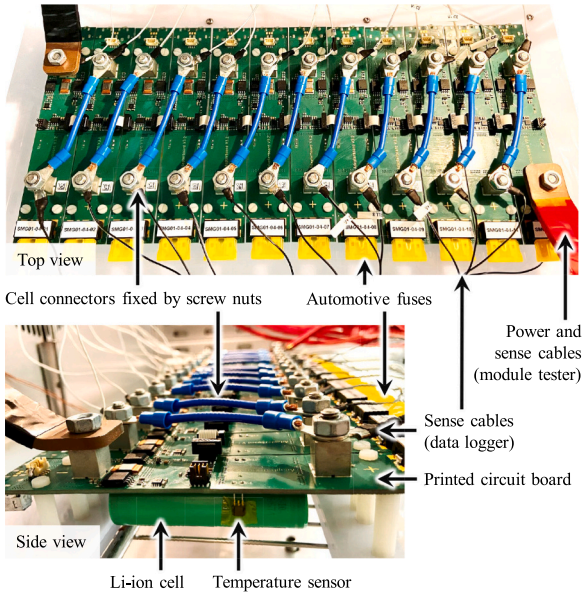

(b) Electrical and mechanical setup of the module

Fig. 1. Experimental setup of the test bench.

temperatures are measured using a Hioki 8423 data logger. The cell voltage resolution is 0.5 mV at a sample rate of 10 Hz. The temperature measurement is only used to keep the cells in their safe operating range. To ensure this, voltage and temperature data is exchanged between the data logger and the module tester, see Fig. 1a.

To enable realistic BEV conditions for the operation of the module, excitation is performed with different driving and charging profiles. The module is alternately discharged using a WLTP[1]-based current profile (maximum currents: −8.26A to 2.02A) and an AU[2]-based current profile (maximum currents: −4.73A to 1.35A). Once the first cell has reached the lower cutoff voltage of 2.5 V, a charge at a rate of 1.5C is performed until the first cell has reached a voltage of 4 V. After another discharge with AU-based and WLTP-based current profiles a standard CCCV[3] charge at a rate of 0.5C follows. The whole procedure is repeated continuously.

To obtain a reproducible ISC with known resistance, emulation is done using an external resistor, as it is a common practice in related studies [24,30,52–54]. Even though in this type of ISC emulation the heat generation occurs outside the jelly roll and the internal cell effects of the ISC are not considered, Zhang et al. [12] confirm that this type of emulation is particularly suitable in the early phase of ISCs. Since only single-cell voltages are required to validate the developed methods for short-circuit detection, this form of electrical emulation is permissible. To cover a wide range of voltage effects [55], the ISC emulation is done with resistors of different magnitudes. The tests are performed successively with resistance values of $R_{ISC} \in \{10\Omega, 100\Omega, 1k\Omega, 10k\Omega\}$ at cell $c = 10$. While the measurements are acquired at a sampling rate of 10 Hz, the methods operate at a rate of 0.1 Hz by averaging over 100 samples. The training of the data model is done in the period from 24 h to 8 h before the occurrence of the ISC. The 8 h before the ISC serve as a validation in the fault-free case.

4. Results and discussion

To establish a relationship between the emulated short circuit resistances R_{ISC} and the Internal Resistances (IR) of the cells, the IRs are determined. Fig. 2 shows the 100ms, DC resistances which were determined using the least squares method. The variations of the IRs between cells are homogeneous over the whole SOC range. In agreement with [26], the cell IR increases in the lower SOC range. Inhomogeneities between cells are mainly observed as offsets between the resistance profiles. The DC IRs at 50% SoC and 25 °C are 24.62mΩ ± 0.31mΩ. Even in the case of the most progressed ISC $R_{ISC} = 10\Omega$, the IR is reduced only to 24.56 mΩ, which corresponds to a change of 0.06mΩ. This change is well below the intercell and SOC- and temperature-induced variations, see [26]. This complicates detection at this early stage using methods based on estimation of the IR [28].

As discussed by Zhang et al. [12], the heat generation at this early stage is also minimal, since the ISC currents are comparatively low. For a fully charged cell with a voltage of 4.2 V and the smallest short-circuit resistance of $R_{ISC} = 10\Omega$ used (largest heat generation), the additional heat generated by the ISC is $P_{ISC} = 1.764$W. For an IR of 24mΩ, the power is comparable to the heat generated when the cell is discharged with a current of 8.6 A, which corresponds to regular operation. Although the temperature rise is measurable in the case of the 10Ω

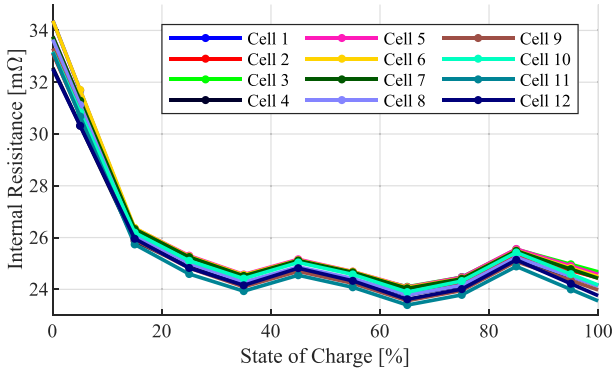

Fig. 2. 100ms, DC resistances of the cells used, over the entire SOC range at 25 °C.

[1] Worldwide harmonized Light vehicles Test Procedure
[2] Artemis Urban
[3] Constant Voltage Constant Current

resistor, it is negligible for the larger short-circuit resistances. The heat generation decreases by an order of magnitude for each of the short-circuit resistors used, to $P_{\mathrm{ISC}} = 0.176\mathrm{W}$ ($R_{\mathrm{ISC}} = 100\Omega$), $P_{\mathrm{ISC}} = 0.018\mathrm{W}$ ($R_{\mathrm{ISC}} = 1\mathrm{k}\Omega$) and $P_{\mathrm{ISC}} = 0.002\mathrm{W}$ ($R_{\mathrm{ISC}} = 10\mathrm{k}\Omega$).

The deviations of the single cell voltages from the median of all 12 cells are shown in Fig. 3. In Fig. 3a, the voltage differences 21 h before and 21 h after the occurrence of the ISC with $R_{\mathrm{ISC}} \in \{10\Omega, 100\Omega, 1\mathrm{k}\Omega, 10\mathrm{k}\Omega\}$ are shown. The time $t = 0\mathrm{h}$ at which the ISC is emulated is marked by a black dashed line. The 11 fault-free cells are shown in black and the faulty cell is marked in red. For comparability of measurements, all plots in Fig. 3a have the same scales. Ideal identical and balanced cells would have a voltage difference of zero. However, although new cells are used, deviations of up to 50 mV are observed before the ISC occurs. These are characteristic deviations in the low SOC range due to the large gradient of the open circuit voltage curve in the low SOC range [26]. For poorly balanced cells or aged cells with capacity differences, these deviations can significantly exceed 50 mV. In the low SOC range, the amplitude can be several 100 mV [18]. After emulation of the ISC, the deviation from the median voltage increases for the affected faulty cell. While a rapid increase in the voltage difference is observed in the 10Ω case, it is hardly observed in the 10 kΩ case. Therefore, in the case of the more progressed 10Ω ISC, the fault would also be observable via threshold-based methods. However, early detection of high-impedance shorts is more challenging. Fig. 3b shows an enlarged section from $t = 0\mathrm{h}$ to $t = 11\mathrm{h}$ after the occurrence of the 1kΩ ISC. Especially in the early phase, the voltage differences caused by the ISC disappear in the usual deviations due to balancing and capacity differences. This makes it difficult to reliably detect ISCs, especially in an early phase.

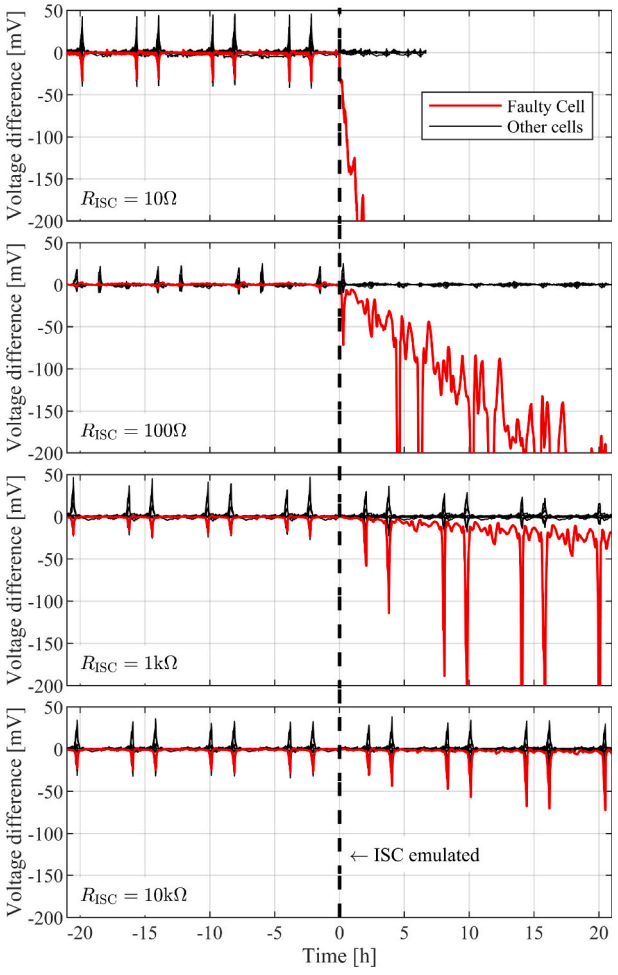

(a) Voltage differences for the cases $R_{\mathrm{ISC}} \in \{10\,\Omega,\ 100\,\Omega,\ 1\,\mathrm{k}\Omega,\ 10\,\mathrm{k}\Omega\}$.

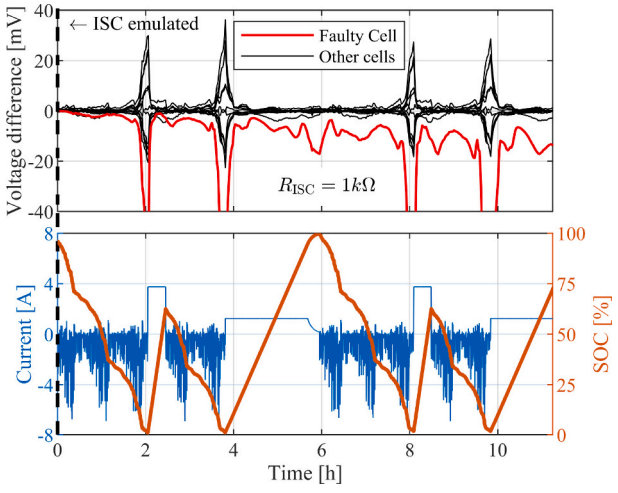

(b) Detail section for case $R_{\mathrm{ISC}} = 1\,\mathrm{k}\Omega$.

Fig. 3. Voltage differences of all cells related to the median voltage, current profile and SOC.

4.1. Choice of training subset

The theoretical derivation regarding the efficient choice of training data from Section 2.4 will be analyzed and discussed in the following based on the measured data. Exemplarily, cell $c = 4$ and the faulty cell $c = 10$ are chosen to be able to visualize the approach in two dimensions. The voltage measurements for the case $R_{\mathrm{ISC}} = 10\mathrm{k}\Omega$ are preprocessed as described in Section 2.2 and the dot products in feature space are calculated. The columns ζ_4 and ζ_{10} of the training data matrix $\boldsymbol{Z}$ are shown in Fig. 4a. In addition, the first $s \in [1,6]$ eigenvalues λ_s, based on all N training points, are given in the plots on the top left corner. In color, the projections of the corresponding kernel principal components $\mathfrak{p}_s$ into the input space are shown. Since the projections are sorted in descending order by the magnitude of the associated eigenvalues, they are unique except for the algebraic sign. As suggested by [40], a combination of a global and a local kernel is used. This mixed kernel allows a high sensitivity for incipient faults and simultaneously a robust behavior for more progressed ISCs [18]. For the example shown in Fig. 4a, a combination of the linear and the Gaussian kernel is used. The global, linear kernel is responsible for contour lines in the form of straight lines. This has the advantage that there is still a gradient in the eigenvectors for points with a large distance to the training data center, as in the case of low impedance shorts (see the $R_{\mathrm{ISC}} = 10\Omega$ case in Fig. 3a). Due to the influence of the local Gaussian kernel, the contour lines are *bent* based on the distribution of the training data. The Gaussian kernel allows for good interpolation behavior due to the high contour line density (large gradient) within the training data, which is necessary for high sensitivity to incipient faults. However, the kernel matrix $\boldsymbol{K}$ to be diagonalized in Eq. (15) has the size 5760×5760 and the online monitoring requires the centering of a 5760-dimensional vector every 10 s, see Eq. (24). Therefore, the goal is to span an approximation of the feature space by a lower number n of training data. In Fig. 4b, the first $j^* \in [1,6]$ points of the subset chosen by Algorithm 1 are highlighted. In addition, the projection of the non-centered kernel vectors.

$$\widetilde{\boldsymbol{k}}_t = \left[\widetilde{\kappa}(\boldsymbol{z}_1, \boldsymbol{z}_{j^*}) \ldots \widetilde{\kappa}(\boldsymbol{z}_t, \boldsymbol{z}_{j^*}) \ldots \widetilde{\kappa}(\boldsymbol{z}_{N_{\mathrm{grid}}}, \boldsymbol{z}_{j^*})\right]^T \in \mathbb{R}^{N_{\mathrm{grid}}}, \tag{56}$$

to the input space with grid points $\boldsymbol{z}_t \in \mathbb{R}^2$ are given in color. The contour lines correspond to constant dot product values. The subset consists of the points with the least linear dependence and therefore comprises the best-suited points to approximate the feature space. Choosing only the $n = 6$ points shown in Fig. 4b as representative of the set of all points

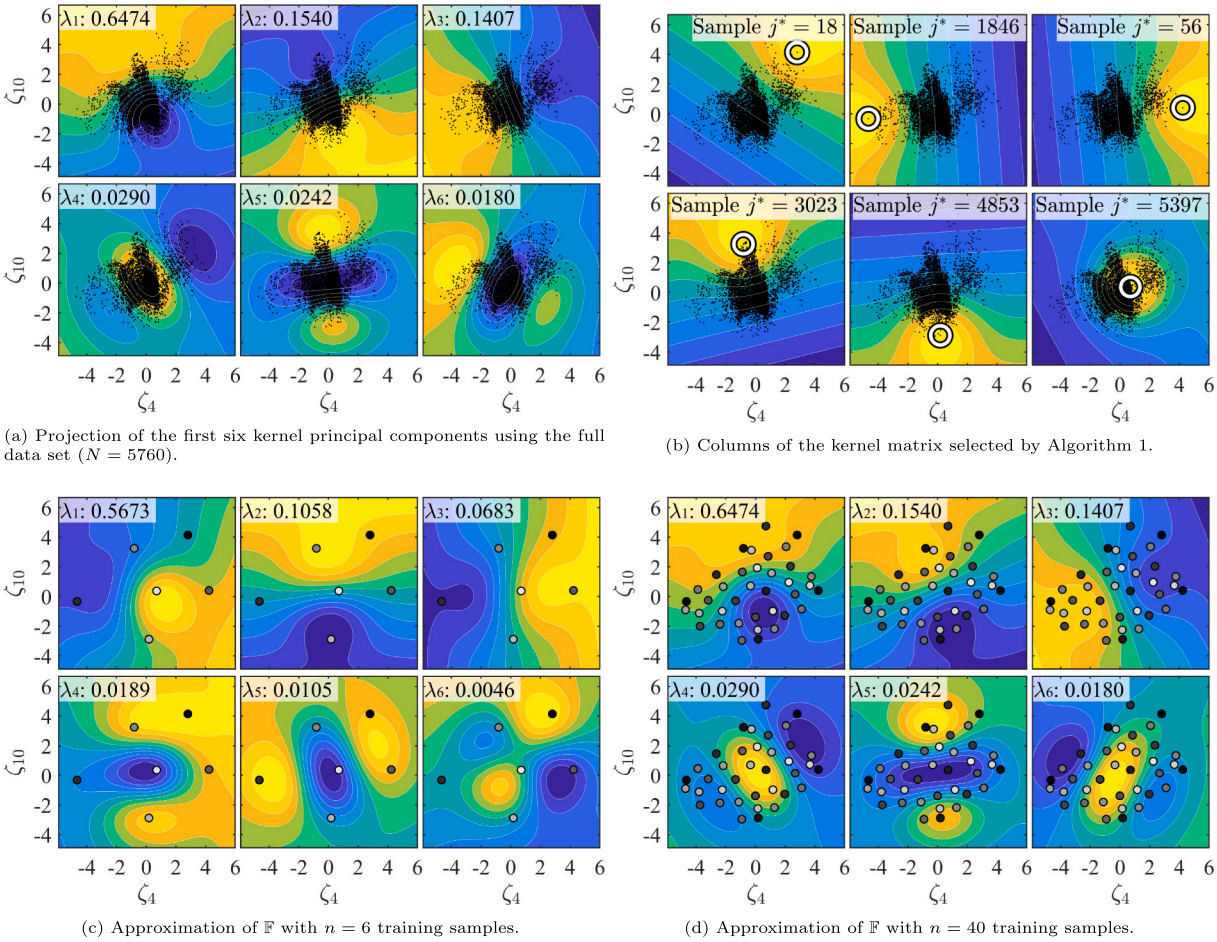

(a) Projection of the first six kernel principal components using the full data set ($N = 5760$).

(b) Columns of the kernel matrix selected by Algorithm 1.

(c) Approximation of $\mathbb{F}$ with $n = 6$ training samples.

(d) Approximation of $\mathbb{F}$ with $n = 40$ training samples.

Fig. 4. Projection of the first six kernel principal components with their associated eigenvalues λ_s (a,c,d) and columns ζ_4 and ζ_{10} of the training data matrix $\boldsymbol{Z}$ (b) for the case $R_{\mathrm{ISC}} = 10\mathrm{k}\Omega$ using a mixed kernel with parameters $\omega_{\mathrm{lin}} = 0.05$ and $\sigma = 1.8$.

results in the kernel principal components and eigenvalues shown in Fig. 4c. The color of the points from black to light gray corresponds to their sorting according to Algorithm 1. The first point is black. Even with the chosen, very small subset of $n = 6$ points, the eigenvalues are in the correct order of magnitude. The shape of the first three kernel principal components is already similar to the contour lines from Fig. 4a. The non-unique sign causes an inversion of the contour colors. In addition, a positive rotation of the kernel PCs is observed. Fig. 4d shows exemplary an approximation with a subset of $n = 40$ points. All six largest eigenvalues already completely match the eigenvalues from Fig. 4a in the first four decimal places. Also, the shape of the kernel principal components largely corresponds to the shape of the kernel principal components based on the full training data, except for the sign. However, the size of the kernel matrix to be stored and diagonalized has been reduced from 5760×5760 to the size 40×40, which corresponds to a reduction by the factor $144^2 = 20736$.

For online monitoring, the T^2- and Q-statistics are calculated according to (26) and (27). The corresponding contour maps for the input space are given in Fig. 5. In Fig. 5a the calculation of the test statistics is based on the full kernel matrix $\boldsymbol{K} \in \mathbb{R}^{5760\times5760}$ and in Fig. 5b the approximation according to Algorithm 1 is used. With a selected tolerance $\eta = 10^{-6}$, $n = 116$ points result. The training data are shown in different shades of blue. In Fig. 5a the training data points are sorted in time, in Fig. 5b the sorting corresponds to the order in which the points are chosen by Algorithm 1, line 6. Dark blue corresponds to the first point or the largest diagonal element. The test points before the occurrence of the ISC are shown in gray. After the occurrence of the ISC of $R_{\mathrm{ISC}} = 10\mathrm{k}\Omega$, the test points are marked in red. For the area shown in green, the respective statistic is below its threshold. The limit, determined by kernel density estimation, is based on a 99% confidence and is shown as a red solid line. Areas above the control limit are represented in red. The union of the green areas of the T^2 and Q statistics is considered fault-free, i.e., a data point is only considered faulty if it is above the threshold for both statistics. The linear kernel is responsible for the global behavior in the form of ellipses [18], since a multivariate normal distribution results for linearly related variables [56]. The local behavior is dominated by the Gaussian kernel based on the distribution of the data. Due to the local kernel, this does not necessarily result in a connected subspace in which the data is evaluated as fault-free. This can be seen in the Q contour map of the training subset. In the example shown, the subspace is not connected even after union of the T^2 and Q subspace. In the case of the full data matrix, 99.32% of the test data lie within the union set of both statistics before the ISC occurs (gray). This corresponds to a False Alarm Rate FAR = 0.68%. The Missed Detection Rate (MDR) within 48 h after the occurrence of the ISC fault is MDR = 26.24%. In the case of the approximation, FAR = 0.16% and MDR = 28.45% result. The fault detection is always a trade-off between low FAR and low MDR or Detection Time (DT). Since the method with the full training set has a lower MDR, but the method with the subset has a lower FAR, the detection performance is considered to be equivalent. Thus, despite the reduction in complexity, no degradation for fault diagnosis is observed.

4.2. *Influence of the mixed kernel parameters*

Based on the $m = 12$ voltage measurements, the influence of the

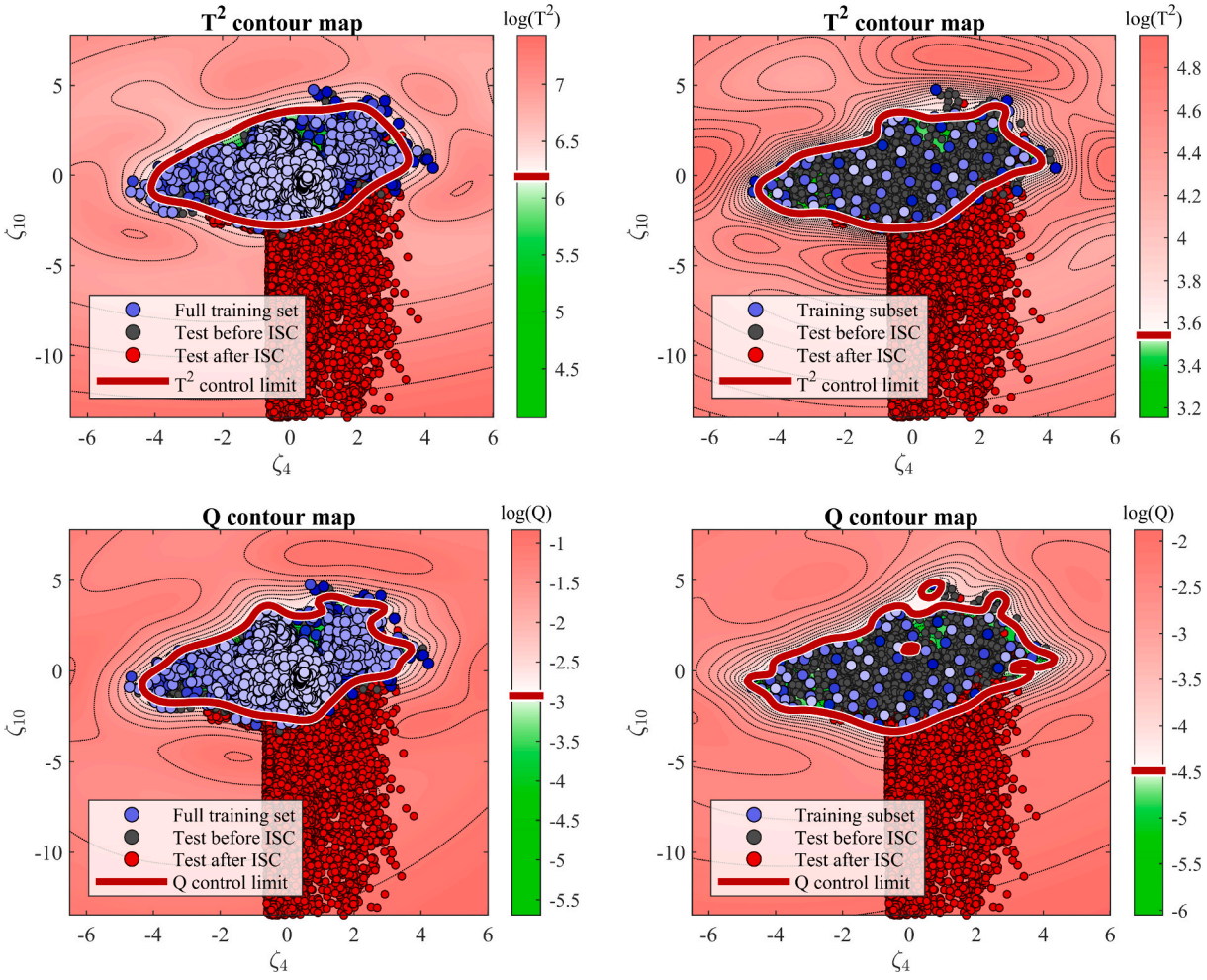

(a) Contour map of the T^2 and Q statistic using the full data set ($N = 5760$).

(b) Contour map of the T^2 and Q statistic after optimal training data selection ($n = 116$).

Fig. 5. Contour maps of the T^2 and Q control statistics in the $\zeta_4\zeta_{10}$-plane based on the full data matrix (a) and the approximation by the incomplete Cholesky decomposition (b). Parameters of the mixed kernel: $\omega_{\text{lin}} = 0.05$ and $\sigma = 1.8$.

weighting of the linear ω_{lin} and Gaussian kernel $\omega_{\text{gauss}} = 1 - \omega_{\text{lin}}$ as well as the influence of the kernel parameter σ is investigated in the following. For this purpose, the methods from Section 2 are applied on the $R_{\text{ISC}} = 10\text{k}\Omega$ data set with different choices of ω_{gauss} and σ. In Fig. 6, the resulting FARs in training and in test as well as the MDR within the first 48 h after the occurrence of the $R_{\text{ISC}} = 10\text{k}\Omega$ fault are shown below each other. Since the training is unsupervised, the MDR is not defined during the training period. For $\omega_{\text{gauss}} = 0$, the method corresponds to the linear PCA monitoring [31]. The linear kernel shows a low FAR in training and in test, but also exhibits a high MDR and DT. For $\omega_{\text{gauss}} = 1$ (pure Gaussian kernel), a low MDR results, but a significant increase in FAR in training and in test is observed. The $\text{FAR}_{\text{train}}$ is due to its definition always less than 1%, the FAR_{test} can exceed 1%, but then indicates an overfitting to the training data. This is especially observable with small σ and high ω_{gauss}. In this case, the low MDR and fast detection time is obtained at the cost of a high FAR. For the range outside $0.8 < \omega_{\text{gauss}} < 1$, $3 < \sigma < 10$, the ratio

$$\frac{\text{FAR}_{\text{test}}}{\text{FAR}_{\text{train}}} \approx 1 \tag{57}$$

holds. A small choice of $\sigma < 3$ leads to a large MDR and small FAR regardless of the weighting ω_{gauss}, comparable to the purely linear behavior for $\omega_{\text{gauss}} = 0$. This can be explained by a strongly disconnected space (see Fig. 5b, Q contour map) where the global behavior of the linear kernel dominates. Except for the extreme values $\omega_{\text{gauss}} \to 1$, $\omega_{\text{gauss}} \to 0$, $\sigma \to 0$, the FAR and MDR exhibit a plateau with a low sensitivity to parameter changes in ω_{gauss} and σ. This indicates a high robustness related to the parameter choice.

To achieve a Pareto-efficient choice of ω_{gauss} and σ, the results from Fig. 6b and C are plotted in Fig. 6d with MDR_{test} on the abscissa and FAR_{test} on the ordinate. The size of the dots corresponds to the values of σ, and the color corresponds to the weighting ω_{gauss}. The contour lines, shown in gray, correspond to constant products of MDR_{test} and FAR_{test}. The goal is to obtain a low MDR_{test} with a simultaneous low FAR_{test}. In Fig. 6d, it can be seen that a higher weighting of the Gaussian kernel tends to result in higher FAR_{test} and lower MDR_{test}. A stronger weighting of the linear kernel has the opposite effect. The yellow dots with $\omega_{\text{gauss}} = 1$ are dominated by points on the Pareto front. This can be explained by the poor extrapolation behavior of the pure Gaussian kernel. As the short-circuit fault progresses and the resulting voltage difference becomes larger, the voltage values are erroneously evaluated as fault-free. A more detailed discussion can be found in [18]. This undesired behavior is reduced by a larger choice of σ. However, the described effect then occurs again with even larger voltage differences. Only a choice of $\omega_{\text{gauss}} < 1$ results in a robust behavior for arbitrarily large voltage differences [40]. Conversely, the purely linear kernel ($\omega_{\text{gauss}} = 0$) with an $\text{MDR}_{\text{test}} = 87.74$ and $\text{FAR}_{\text{test}} = 0.17$ is also not Pareto optimal. Since the choice of σ has no effect on the detection performance in the

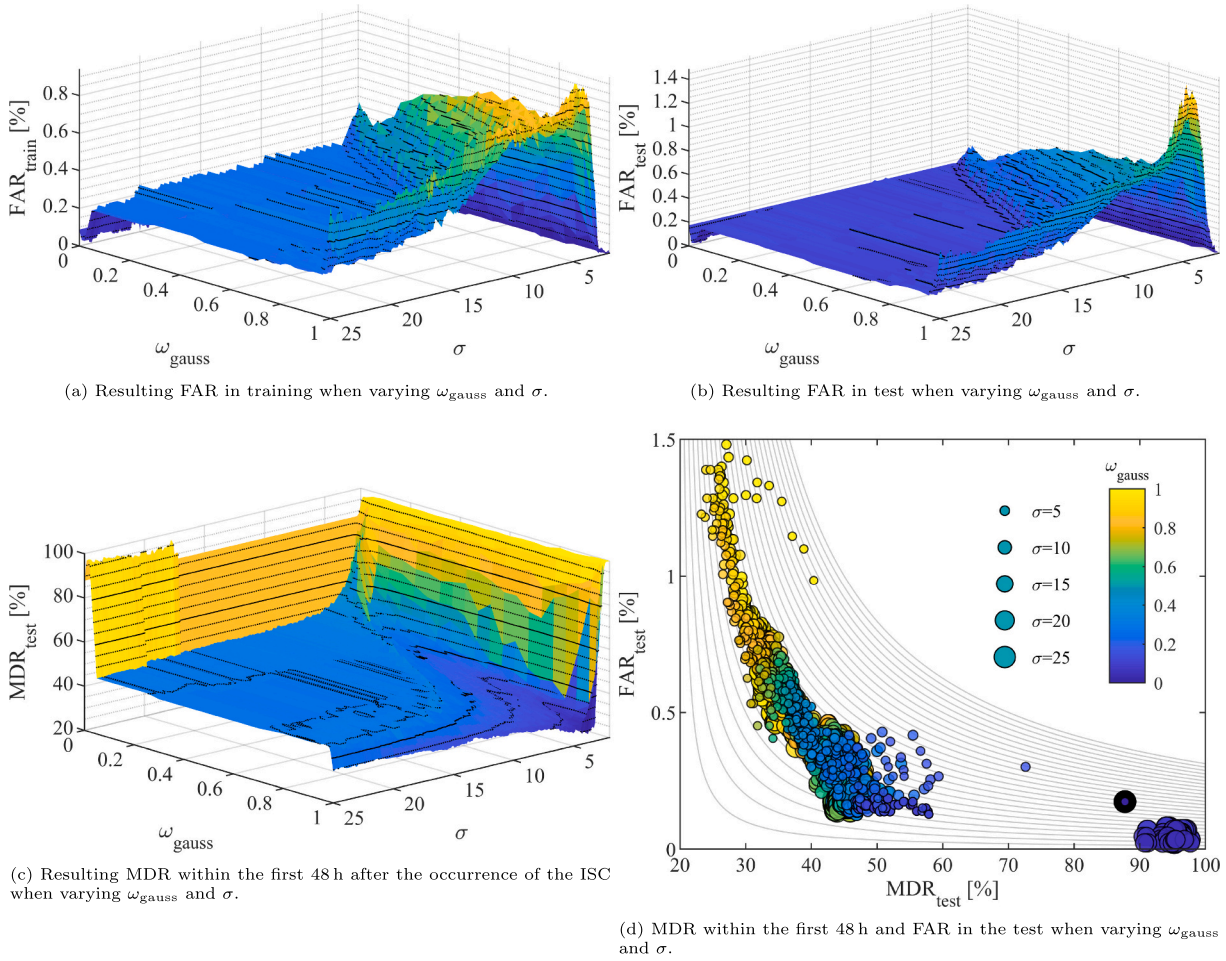

(a) Resulting FAR in training when varying ω_{gauss} and σ.

(b) Resulting FAR in test when varying ω_{gauss} and σ.

(c) Resulting MDR within the first 48 h after the occurrence of the ISC when varying ω_{gauss} and σ.

(d) MDR within the first 48 h and FAR in the test when varying ω_{gauss} and σ.

Fig. 6. Influence of a variation of the weight ω_{gauss} and the kernel parameter σ on the resulting FAR in training and in test as well as the MDR.

case $\omega_{\text{gauss}} = 0$, the points for all σ lie on top of each other. In general, a larger kernel parameter σ contributes to a smaller FDR and higher MDR, and vice versa. The plateau from Fig. 6a-c is seen in Fig. 6d by a high density of points in the range $40 < \text{MDR}_{\text{test}} < 50$ and $0.1 < \text{FAR}_{\text{test}} < 0.4$. This confirms the low sensitivity of the method to parameter changes in ω_{gauss} and σ for non-extreme parameter values. The plateau generally exhibits low FAR and MDR. Based on the sensitivity analysis, the parameters $\sigma = 20.3$ and $\omega_{\text{gauss}} = 0.55$ are chosen.

Fig. 7 shows the decrease of the sum of the diagonal elements $\sum_{j=\tau}^{N} \boldsymbol{G}_{jj}$ during the execution of Algorithm 1, depending on the size of the training subset n and the number of dimensions m. With a constant number of training points, it is observed that the distribution of the data can be approximated worse for an increasing number of dimensions. This effect is called curse of dimensionality [57,58]. For the first points, however, a rapid decrease in $\sum_{j=\tau}^{N} \boldsymbol{G}_{jj}$ is achieved. This is due to the linear kernel. In the case of the linear kernel the feature space is already completely spanned by $n = m$ linear independent vectors. Thus, for a choice of $n \geq m$ at least the detection performance of the linear method can be guaranteed. This makes the method robust against a high number of voltage signals, as they are present in large battery packs. The addition of further points ($n > m$) improves the detection performance due to the influence of the Gaussian kernel.

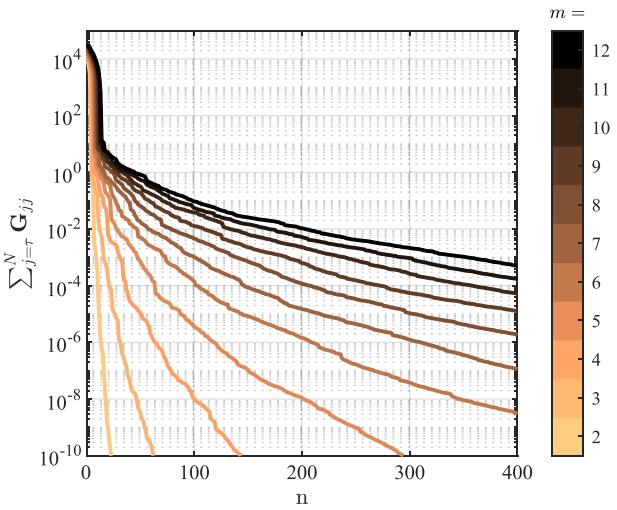

Fig. 7. Decrease of the sum of diagonal elements of $\boldsymbol{G}$ (tolerance η), depending on the training subset n and the number of dimensions m (total number of cells).

4.3. Application of the framework for ISC diagnosis

Fig. 8 shows the results after applying the procedure from Section 2 to diagnose soft ISCs. Fig. 8a shows the values of the T^2 and Q statistics and the Upper Control Limit (UCL) based on a kernel density estimation with a confidence of 99%. First, the method is validated on fault-free measurement data. The training is done in the first 16 h, the test starts for $t >$ 16h. The selected training subset has a cardinality of $n = 257$ given a tolerance of $\eta = 10^{-3}$. The training points are marked in blue. In addition, the values of the two test statistics are calculated for the remaining training points and test points (red). The FARs are $\text{FAR}_{\text{train}} =$

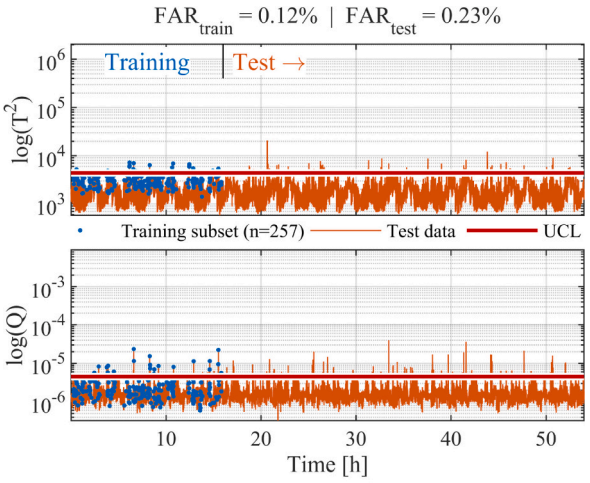

(a) T^2 and Q statistic for the fault-free validation case.

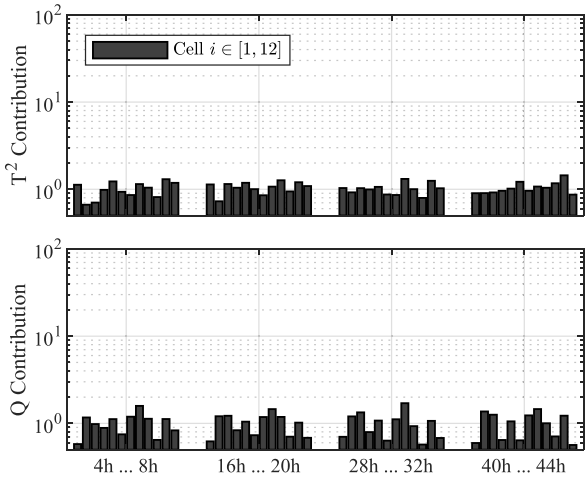

(b) Contribution plots for the control statistics shown in Fig. 8a.

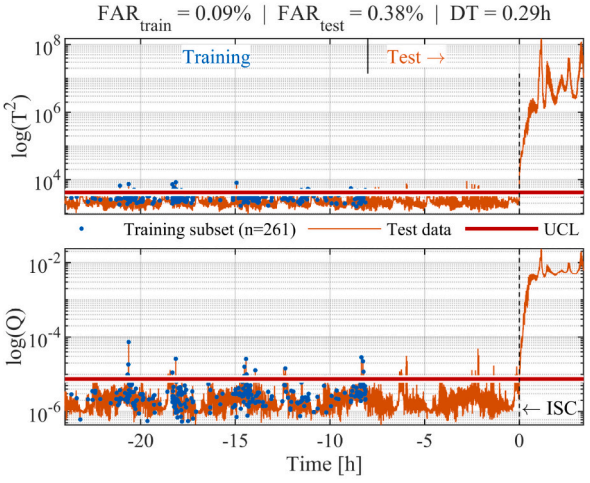

(c) T^2 and Q statistic for the case $R_{\mathrm{ISC}} = 10\,\Omega$.

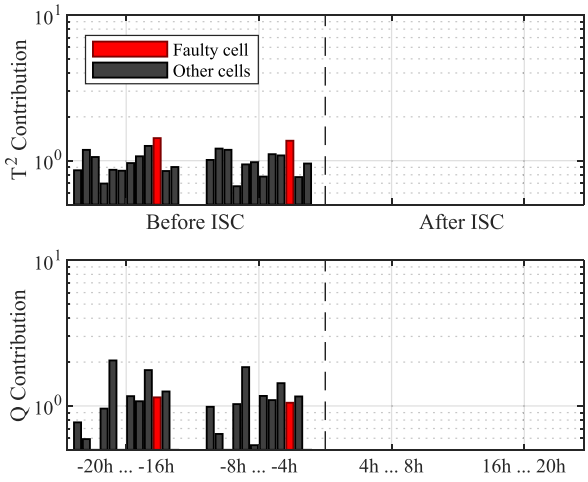

(d) Contribution plots for the control statistics shown in Fig. 8c.

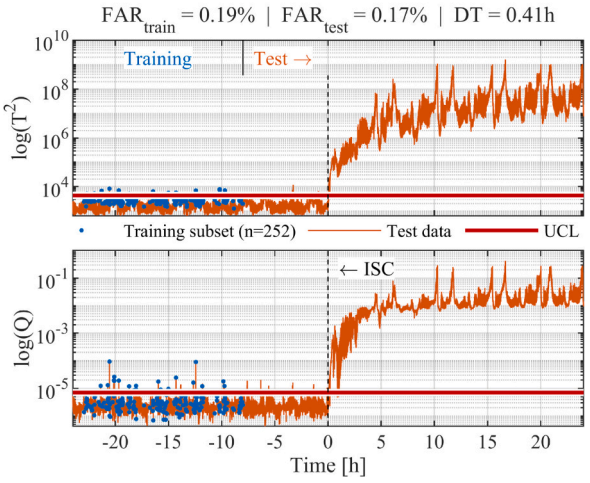

(e) T^2 and Q statistic for the case $R_{\mathrm{ISC}} = 100\,\Omega$.

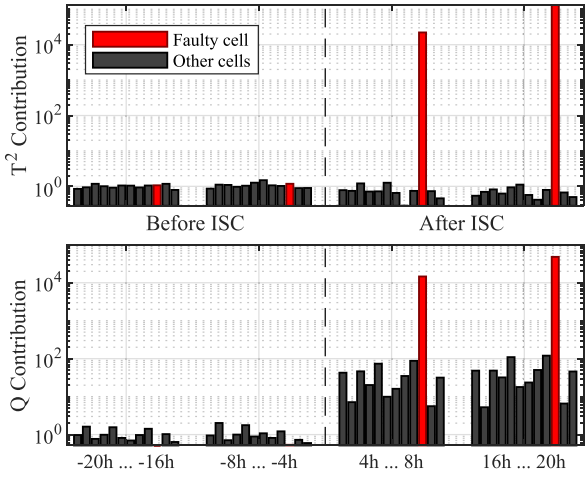

(f) Contribution plots for the control statistics shown in Fig. 8e.

Fig. 8. Resulting T^2 and Q control statistics after application of the KPCA-based monitoring scheme with optimal training data selection (precision $\eta = 10^{-3}$) for the cases $R_{\mathrm{ISC}} \in \{10\Omega, 100\Omega, 1\mathrm{k}\Omega, 10\mathrm{k}\Omega\}$, as well as the corresponding contribution plots for different time periods.

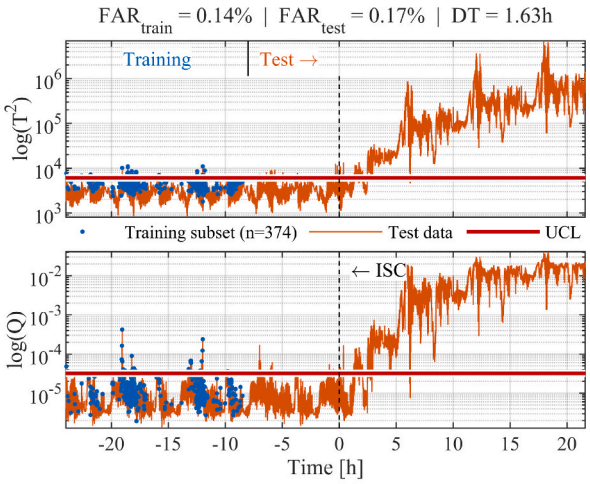

(g) T^2 and Q statistic for the case $R_{\mathrm{ISC}} = 1\,\mathrm{k\Omega}$.

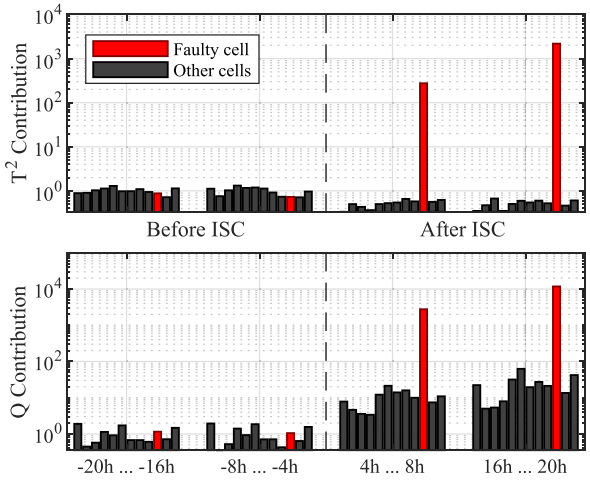

(h) Contribution plots for the control statistics shown in Fig. 8g.

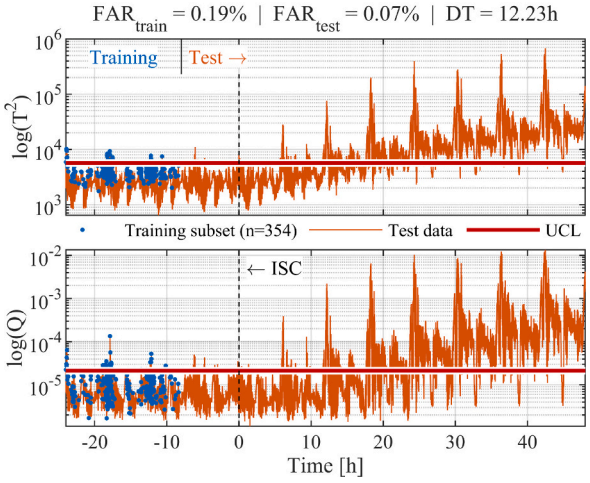

(i) T^2 and Q statistic for the case $R_{\mathrm{ISC}} = 10\,\mathrm{k\Omega}$.

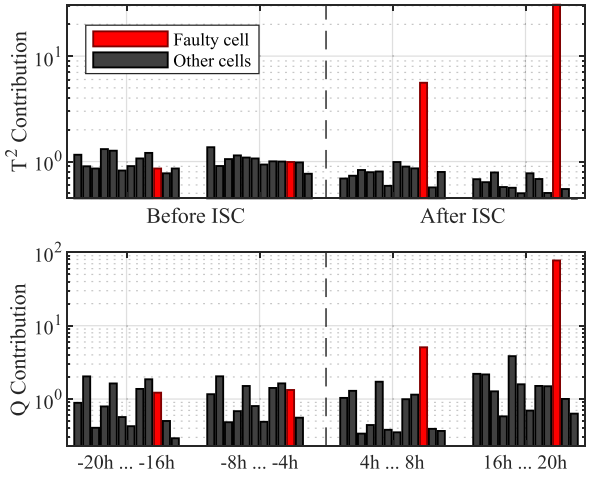

(j) Contribution plots for the control statistics shown in Fig. 8i.

Fig. 8. (*continued*).

0.12% and $\mathrm{FAR}_{\mathrm{test}} = 0.23\%$. No drift is observed in the statistics. Fig. 8b shows the contributions calculated according to Section 2.5 for different time periods. Each bar corresponds to one of the $m = 12$ cells. The contribution plots show the contribution of each variable to the T^2 and Q statistics, respectively. The average of the contributions is normalized to 1 in training. No significant change is observed in the test data for the further periods after training, which corresponds to the desired behavior in the fault-free case.

Fig. 8c,f,h,j show the results for the fault cases $R_{\mathrm{ISC}} \in \{10\Omega, 100\Omega, 1\mathrm{k}\Omega, 10\mathrm{k}\Omega\}$. Before the ISC occurs at time $t = 0$h, indicated by a dashed line, 16 h of training and 8 h of validation are performed. The number of points chosen to approximate the feature space at a tolerance of $\eta = 10^{-3}$ ranges from $n = 252$ to $n = 357$. This corresponds to 019% to 038% of the size of the full kernel matrix, which means a significant reduction in computational and storage complexity. The FARs in training and testing range from 0.14% to 0.19%. The DT depends on the magnitude of the ISC. Smaller resistances produce a high voltage difference more quickly, see Fig. 3. The definition of DT is analogous to [18]. The detection measure takes the value 1 if both statistics are above their UCL and is 0 otherwise. The detection measure is filtered in time by a moving average filter with a time window of 200 samples, which corresponds to 0.56 h. If the detection measure exceeds a threshold value of 0.5, the fault is considered detected. The moving average filter delays the DT but prevents undesired false alarms. Low short-circuit resistances are also observable by the pure voltage difference (see Fig. 3a, $R_{\mathrm{ISC}} = 10\Omega$) or, in the case of even more progressed ISC faults, by a temperature rise.

The corresponding contribution plots are shown in Fig. 8d,f,h,j. A period during training ($t \in [-20\mathrm{h}, -16\mathrm{h}]$) and a period during the validation phase ($t \in [-8\mathrm{h}, -4\mathrm{h}]$) is shown to the left of the dashed line. The two periods to the right of the dashed line are chosen after ISC triggering. The cell $c = 10$ for which an ISC is emulated at $t = 0$h is highlighted in red. As in Fig. 8b, no significant contribution of a single cell to the respective statistics is observed before the occurrence of the fault. However, after the occurrence of the ISC, the contribution to the respective statistics is dominated by the faulty cell. In the case of more progressed ISCs with significant heat generation, the additional temperature anomaly would also be expected to cause a slightly increased contribution from the neighboring cells of a battery pack. However, this is not observed in the contribution plots shown, since the ISC is emulated purely electrically and therefore does not affect serial cells. Although in the case of the $R_{\mathrm{ISC}} = 10\mathrm{k}\Omega$ the fault is detected only after 12.23 h, the contribution of the faulty cell is already significant in the period $t \in [-8\mathrm{h}, -4\mathrm{h}]$. Cell 10 already shows 5.65 times the contribution to the T^2 statistic and 2.95 times the contribution to the Q statistic compared to the next largest contribution of cell 7 and cell 5, respectively. The

method from Section 2.5 can thus be successfully applied to mixed kernels and the resulting contribution plots are suitable for isolating the faulty cell.

Moreover, it is observed that after the fault occurs, the contribution of the fault-free cells shifts from the T^2 statistic to the Q statistic. According to [44], the T^2 statistic is associated with systematic variations in the training data. The Q statistic, in contrast, monitors the non-systematic part in the training data. It is therefore associated with the noise or unexpected events in the test data. After the occurrence of the fault, the behavior of the voltage signals no longer corresponds to the learned data model, which is why the mean contributions to the T^2 statistics decrease and the mean contributions to the Q statistics increase.

5. Conclusion

The present study compares the differences of single cell voltages to diagnose ISCs. Since the cell voltage differences interact nonlinearly, a nonlinear data model is learned using KPCA and applied for a cross-cell monitoring. The use of mixed kernel functions enables both high sensitivity for soft ISCs and high robustness of the method in the case of more progressed, low-impedance ISCs. The approach is validated on an experimental battery module with a wide range of short-circuit resistances in the range from 10Ω to 10kΩ. Compared to the linear methods, nonlinear monitoring requires more computational effort. While the quadratic covariance matrix calculated for linear monitoring has the dimension m of the input variables, the quadratic Gram matrix in the nonlinear case has the dimension N of the number of samples. However, an analysis of the distribution in the high-dimensional feature space shows that the projected vectors have linear dependencies. Therefore, the resulting subspace can also be spanned with a subset $n \ll N$ of training data. Further reduction yields an approximation of the Gram matrix to a desired accuracy. As discussed in this study, a choice of $n = m$ samples guarantees at least the performance of the linear method. For the application shown, the optimal training data selection reduces the size of the kernel matrix to 0.19% to 0.38% of the size of the full kernel matrix, which significantly reduces the computational cost. The optimal choice of parameters results in a Pareto optimization between the FAR and the MDR. It is shown that only combinations of the linear and the Gaussian kernel are optimal. The detection performance, i.e., the compromise of FAR and MDR, is thereby robust away from extremely chosen parameters (purely linear, purely Gaussian, or very small Gaussian kernel). The contribution analysis for mixed kernels, developed for fault isolation, allows localization of the faulty cell. The optimized nonlinear method allows detection of an emulated 10kΩ ISC in a 12s1p module consisting of 2.5 Ah cells after 12.23 h. However, in the contributions to the control statistics, significant contributions of the defective cell are already detectable in the period $t \in [4\text{h}, 8\text{h}]$ after emulation of the ISC.

CRediT authorship contribution statement

Michael Schmid: Conceptualization, Methodology, Software, Validation, Formal analysis, Investigation, Resources, Data curation, Writing – original draft, Writing – review & editing, Visualization. **Christian Endisch:** Project administration, Funding acquisition.

Declaration of competing interest

The authors declare the following financial interests/personal relationships which may be considered as potential competing interests: This work was funded by the AUDI AG within the scope of an ongoing research project.

Acknowledgment

The authors would like to express their very great appreciation to Dr. M. Hinterberger (AUDI AG) for his constructive support and valuable expert advice during the planning and development of this research work. We also thank Dr. Lidiya Komsiyska (Technische Hochschule Ingolstadt) for her constructive comments on the manuscript and Sascha Speer (Technische Hochschule Ingolstadt) for providing hardware components that were used for the experimental investigations. We acknowledge support by the Open Access Publication Fund of Technische Hochschule Ingolstadt.

References

[1] Süddeutsche Zeitung, Automesse iaa mobility: Klimaneutralität im mittelpunkt, URL, https://sz.de/dpa.urn-newsml-dpa-com-20090101-210830-99-22626, 2021.
[2] W. Gao, X. Li, M. Ma, Y. Fu, J. Jiang, C. Mi, Case study of an electric vehicle battery thermal runaway and online internal short-circuit detection, IEEE Trans. Power Electron. 36 (3) (2021) 2452–2455, https://doi.org/10.1109/TPEL.2020.3013191.
[3] R. Xiong, S. Ma, H. Li, F. Sun, J. Li, Toward a safer battery management system: a critical review on diagnosis and prognosis of battery short circuit, iScience 23 (4) (2020), 101010, https://doi.org/10.1016/j.isci.2020.101010.
[4] X. Feng, M. Ouyang, X. Liu, L. Lu, Y. Xia, X. He, Thermal runaway mechanism of lithium ion battery for electric vehicles: a review, Energy Storage Mater. 10 (2018) 246–267, https://doi.org/10.1016/j.ensm.2017.05.013.
[5] H. Maleki, J.N. Howard, Internal short circuit in li-ion cells, J. Power Sources 191 (2) (2009) 568–574, https://doi.org/10.1016/j.jpowsour.2009.02.070.
[6] M. Shen, Q. Gao, A review on battery management system from the modeling efforts to its multiapplication and integration, Int. J. Energy Res. 43 (10) (2019) 5042–5075, https://doi.org/10.1002/er.4433.
[7] L. Lu, X. Han, J. Li, J. Hua, M. Ouyang, A review on the key issues for lithium-ion battery management in electric vehicles, J. Power Sources 226 (2013) 272–288, https://doi.org/10.1016/j.jpowsour.2012.10.060.
[8] X. Hu, K. Zhang, K. Liu, X. Lin, S. Dey, S. Onori, Advanced fault diagnosis for lithium-ion battery systems: a review of fault mechanisms, fault features, and diagnosis procedures, IEEE Ind. Electron. Mag. 14 (3) (2020) 65–91, https://doi.org/10.1109/MIE.2020.2964814.
[9] J. Hu, Z. Wei, H. He, An online adaptive internal short circuit detection method of lithium-ion battery, Automotive Innovation 4 (1) (2021) 93–102, https://doi.org/10.1007/s42154-020-00127-9.
[10] J. Hu, H. He, Z. Wei, Y. Li, Disturbance-immune and aging-robust internal short circuit diagnostic for lithium-ion battery, IEEE Trans. Ind. Electron. 69 (2) (2022) 1988–1999, https://doi.org/10.1109/TIE.2021.3063968.
[11] X. Lai, C. Jin, W. Yi, X. Han, X. Feng, Y. Zheng, M. Ouyang, Mechanism, modeling, detection, and prevention of the internal short circuit in lithium-ion batteries: recent advances and perspectives, Energy Storage Mater. 35 (2021) 470–499, https://doi.org/10.1016/j.ensm.2020.11.026.
[12] G. Zhang, X. Wei, X. Tang, J. Zhu, S. Chen, H. Dai, Internal short circuit mechanisms, experimental approaches and detection methods of lithium-ion batteries for electric vehicles: a review, Renew. Sust. Energ. Rev. 141 (2021), 110790, https://doi.org/10.1016/j.rser.2021.110790.
[13] M. Zhang, M. Ouyang, L. Lu, X. He, X. Feng, L. Liu, X. Xie, Battery internal short circuit detection, ECS Trans. 77 (11) (2017) 217–223, https://doi.org/10.1149/07711.0217ecst.
[14] Y. Pan, X. Feng, M. Zhang, X. Han, L. Lu, M. Ouyang, Internal short circuit detection for lithium-ion battery pack with parallel-series hybrid connections, J. Clean. Prod. 255 (2020), 120277, https://doi.org/10.1016/j.jclepro.2020.120277.
[15] M. Zhang, J. Du, L. Liu, J. Siegel, L. Lu, X. He, M. Ouyang, Internal short circuit detection method for battery pack based on circuit topology, Sci. China Technol. Sci. 61 (10) (2018) 1502–1511, https://doi.org/10.1007/s11431-017-9299-3.
[16] L. Komsiyska, T. Buchberger, S. Diehl, M. Ehrensberger, C. Hanzl, C. Hartmann, M. Hölzle, J. Kleiner, M. Lewerenz, B. Liebhart, M. Schmid, D. Schneider, S. Speer, J. Stöttner, C. Terbrack, M. Hinterberger, C. Endisch, Critical review of intelligent battery systems: challenges, implementation, and potential for electric vehicles, Energies 14 (18) (2021) 5989, https://doi.org/10.3390/en14185989.
[17] M. Schmid, E. Gebauer, C. Endisch, Structural analysis in reconfigurable battery systems for active fault diagnosis, IEEE Trans. Power Electron. 36 (8) (2021) 8672–8684, https://doi.org/10.1109/TPEL.2021.3049573.
[18] M. Schmid, B. Liebhart, J. Kleiner, C. Endisch, R. Kennel, Online detection of soft internal short circuits in lithium-ion battery packs by data-driven cell voltage monitoring, in: 2021 IEEE 12th Energy Conversion Congress & Exposition - Asia (ECCE-Asia), IEEE, 2021, pp. 1711–1718, https://doi.org/10.1109/ECCE-Asia49820.2021.9479175.
[19] B. Xia, Y. Shang, T. Nguyen, C. Mi, A correlation based fault detection method for short circuits in battery packs, J. Power Sources 337 (2017) 1–10, https://doi.org/10.1016/j.jpowsour.2016.11.007.
[20] Y. Shang, G. Lu, Y. Kang, Z. Zhou, B. Duan, C. Zhang, A multi-fault diagnosis method based on modified sample entropy for lithium-ion battery strings, J. Power Sources 446 (2020), 227275, https://doi.org/10.1016/j.jpowsour.2019.227275.
[21] B. Yang, N. Cui, M. Wang, Internal short circuit fault diagnosis for lithiumion battery based on voltage and temperature, in: 2019 3rd Conference on Vehicle

Control and Intelligence (CVCI), IEEE, 2019, pp. 1–6, https://doi.org/10.1109/CVCI47823.2019.8951717.
[22] Y. Zheng, W. Gao, M. Ouyang, L. Lu, L. Zhou, X. Han, State-of-charge inconsistency estimation of lithium-ion battery pack using mean-difference model and extended kalman filter, J. Power Sources 383 (2018) 50–58, https://doi.org/10.1016/j.jpowsour.2018.02.058.
[23] M. Seo, T. Goh, M. Park, S. Kim, Detection method for soft internal short circuit in lithium-ion battery pack by extracting open circuit voltage of faulted cell, Energies 11 (7) (2018) 1669, https://doi.org/10.3390/en11071669.
[24] X. Lai, W. Yi, X. Kong, X. Han, L. Zhou, T. Sun, Y. Zheng, Online detection of early stage internal short circuits in series-connected lithium-ion battery packs based on state-of-charge correlation, J. Energy Storage 30 (2020), 101514, https://doi.org/10.1016/j.est.2020.101514.
[25] X. Kong, Y. Zheng, M. Ouyang, L. Lu, J. Li, Z. Zhang, Fault diagnosis and quantitative analysis of micro-short circuits for lithium-ion batteries in battery packs, J. Power Sources 395 (2018) 358–368, https://doi.org/10.1016/j.jpowsour.2018.05.097.
[26] M. Schmid, U. Vögele, C. Endisch, A novel matrix-vector-based framework for modeling and simulation of electric vehicle battery packs, J. Energy Storage 32 (2020), 101736, https://doi.org/10.1016/j.est.2020.101736.
[27] H. Nakajima, T. Kitahara, Diagnosis method to detect the incorporation of metallic particles in a lithium ion battery, ECS Trans. 68 (2) (2015) 59–74, https://doi.org/10.1149/06802.0059ecst.
[28] X. Kong, G.L. Plett, M. Scott Trimboli, Z. Zhang, D. Qiao, T. Zhao, Y. Zheng, Pseudo-two-dimensional model and impedance diagnosis of micro internal short circuit in lithium-ion cells, J.Energy Storage 27 (2020), 101085, https://doi.org/10.1016/j.est.2019.101085.
[29] J. Xu, H. Wang, H. Shi, X. Mei, Multi-scale short circuit resistance estimation method for series connected battery strings, Energy 202 (2020), 117647, https://doi.org/10.1016/j.energy.2020.117647.
[30] M. Seo, M. Park, Y. Song, S.W. Kim, Online detection of soft internal short circuit in lithium-ion batteries at various standard charging ranges, IEEE Access 8 (2020) 70947–70959, https://doi.org/10.1109/ACCESS.2020.2987363.
[31] M. Schmid, H.-G. Kneidinger, C. Endisch, Data-driven fault diagnosis in battery systems through cross-cell monitoring, IEEE Sensors J. 21 (2) (2021) 1829–1837, https://doi.org/10.1109/JSEN.2020.3017812.
[32] M. Schmid, J. Kleiner, C. Endisch, Early detection of internal short circuits in series-connected battery packs based on nonlinear process monitoring, J.Energy Storage 48 (2022), 103732, https://doi.org/10.1016/j.est.2021.103732.
[33] B. Schölkopf, A. Smola, K.-R. Müller, Nonlinear component analysis as a kernel eigenvalue problem, Neural Comput. 10 (5) (1998) 1299–1319, https://doi.org/10.1162/089976698300017467.
[34] J.-M. Lee, C. Yoo, S.W. Choi, P.A. Vanrolleghem, I.-B. Lee, Nonlinear process monitoring using kernel principal component analysis, Chem. Eng. Sci. 59 (1) (2004) 223–234, https://doi.org/10.1016/j.ces.2003.09.012.
[35] H. Abdi, L.J. Williams, Principal component analysis, Wiley Interdiscip. Rev. Comput. Stat. 2 (4) (2010) 433–459, https://doi.org/10.1002/wics.101.
[36] B. Schölkopf, A. Smola, K.-R. Müller, Kernel principal component analysis, in: International Conference on Artificial Neural Networks 1327, 1997, pp. 583–588, https://doi.org/10.1007/BFb0020217.
[37] S.S. Haykin, Neural Networks: A Comprehensive Foundation, 2nd Edition, Prentice Hall and Prentice-Hall International, Upper Saddle River, NJ and London, 1999.
[38] B.E. Boser, I.M. Guyon, V.N. Vapnik, A training algorithm for optimal margin classifiers, in: D. Haussler (Ed.), Proceedings of the Fifth Annual Workshop on Computational Learning Theory, ACM, New York, NY, 1992, pp. 144–152, https://doi.org/10.1145/130385.130401.
[39] N. Cristianini, J. Shawe-Taylor, An Introduction to Support Vector Machines: And Other Kernel-Based Learning Methods, Cambridge University Press, Cambridge and New York, 2000, https://doi.org/10.1017/CBO9780511801389.
[40] K.E.S. Pilario, Y. Cao, M. Shafiee, Mixed kernel canonical variate dissimilarity analysis for incipient fault monitoring in nonlinear dynamic processes, Comput. Chem. Eng. 123 (2019) 143–154, https://doi.org/10.1016/j.compchemeng.2018.12.027.
[41] C.R. Souza, Kernel functions for machine learning applications, URL, http://crsouza.blogspot.com/2010/03/kernel-functions-for-machine-learning.html, 2010.
[42] K. E. S. Pilario M. Shafiee, Mixed Kernel Functions for Multivariate Statistical Monitoring of Nonlinear Processes. doi:10.1007/978-3-030-57745-2_6.
[43] S. Altmannshofer, C. Endisch, J. Martin, M. Gerngross, R. Limbacher, Robust estimation of vehicle longitudinal dynamics parameters, in: 2016 IEEE Intelligent Vehicles Symposium (IV), Piscataway, NJ, 2016, pp. 566–571, https://doi.org/10.1109/IVS.2016.7535443.
[44] D. Slišković, R. Grbić, Ž. Hocenski, Multivariate statistical process monitoring, Tehnički Vjesnik 19 (1) (2012) 33–41.
[45] S. Yin, S.X. Ding, X. Xie, H. Luo, A review on basic data-driven approaches for industrial process monitoring, IEEE Trans. Ind. Electron. 61 (11) (2014) 6418–6428, https://doi.org/10.1109/TIE.2014.2301773.
[46] G. Baudat, F. Anouar, Kernel-based methods and function approximation, in: IJCNN'01, IEEE, Piscataway, N.J, 2001, pp. 1244–1249, https://doi.org/10.1109/IJCNN.2001.939539.
[47] H. Wang, Z. Hu, Y. Zhao, Kernel principal component analysis for large scale data set, in: International Conference on Intelligent Computing 4113, 2006, pp. 745–756, https://doi.org/10.1007/11816157_91.
[48] F.R. Bach, M.I. Jordan, Kernel independent component analysis, J. Mach. Learn. Res. 3 (2003) 1–48, https://doi.org/10.1162/153244303768966085.
[49] A.J. Smola, B. Schölkopf, Sparse greedy matrix approximation for machine learning, in: Proceedings of the 17. International Conference on Machine Learning, 2000, pp. 911–918.
[50] C.K.I. Williams, M. Seeger, Using the nyström method to speed up kernel machines, Adv. Neural Inf. Proces. Syst. 13 (2000) 682–688.
[51] X. Deng, X. Tian, A new fault isolation method based on unified contribution plots, in: Proceedings of the 30th Chinese Control Conference, 2011, pp. 4280–4285.
[52] M. Ouyang, M. Zhang, X. Feng, L. Lu, J. Li, X. He, Y. Zheng, Internal short circuit detection for battery pack using equivalent parameter and consistency method, J. Power Sources 294 (2015) 272–283, https://doi.org/10.1016/j.jpowsour.2015.06.087.
[53] Y. Zheng, Y. Lu, W. Gao, X. Han, X. Feng, M. Ouyang, Micro-short-circuit cell fault identification method for lithium-ion battery packs based on mutual information, IEEE Trans. Ind. Electron. 68 (5) (2021) 4373–4381, https://doi.org/10.1109/TIE.2020.2984441.
[54] W. Gao, Y. Zheng, M. Ouyang, J. Li, X. Lai, X. Hu, Micro-short-circuit diagnosis for series-connected lithium-ion battery packs using mean-difference model, IEEE Trans. Ind. Electron. 66 (3) (2019) 2132–2142, https://doi.org/10.1109/TIE.2018.2838109.
[55] B. Liu, Y. Jia, C. Yuan, L. Wang, X. Gao, S. Yin, J. Xu, Safety issues and mechanisms of lithium-ion battery cell upon mechanical abusive loading: a review, Energy Storage Mater. 24 (2020) 85–112, https://doi.org/10.1016/j.ensm.2019.06.036.
[56] E. Vanhatalo, Multivariate process monitoring of an experimental blast furnace, Qual. Reliab. Eng. Int. 26 (5) (2010) 495–508, https://doi.org/10.1002/qre.1070.
[57] R. Bellmann, Combinatorial processes and dynamic programming, in: Proceedings of the Tenth Symposium in Applied Mathematics of The American Mathematical Society, 1958.
[58] R.B. Marimont, M.B. Shapiro, Nearest neighbour searches and the curse of dimensionality, IMA J. Appl. Math. 24 (1) (1979) 59–70, https://doi.org/10.1093/imamat/24.1.59.